

Reply to editor - Drivers of Pine Island Glacier speed-up between 1996 and 2016.

Jan De Rydt, Ronja Reese, Fernando S. Paolo, G. Hilmar Gudmundsson

November 11, 2020

Dear Andreas,

Thank you for your response and the opportunity to submit a revised manuscript. We greatly appreciate your detailed report, and value your request to make additional changes to the manuscript. A point-by-point response to your comments and list of substantial reviewer comments with reference to changes in the manuscript are provided below. Our replies are in *blue italic* and all line numbers refer to the manuscript with tracked changes, included at the end of this document. We hope to have addressed all questions and concerns more explicitly now.

Yours sincerely,

Jan De Rydt on behalf of the authors

Reply to editor comments

Editor: “Dear Jan de Rydt and co-authors, Your manuscript received 3 thorough and in general positive reviews that highlighted the quality and originality and the relevance and added value of the manuscript with regard to analysis and understanding of the observed dynamic changes at Pine Island Glacier over the last two decades. A all referees agreed that this research and manuscript would valuable contribution to TC and should be published after some revisions.

However, besides quite a few rather minor editing corrections the referees also raised some more substantial points which mainly concerned in brief:

- critical points and further discussion on the joined optimization of A (ice rheology) and C (slipperiness)
- related the robustness of the inversions
- clarification of data quality
- clarification of interaction of grounding line and thinning in optimization
- aspects of eqn 2
- some updating and improvement in the reference to existing literature

Below we explain how and where we have addressed each of these substantial points in the manuscript. For ease of reference we number them as follows:

- *C1: further discussion on the optimization of A and C (raised by Refs 1 and 3).*
- *C2: robustness of the inversions (raised by Refs 1 and 3)*
- *C3: quality of the 1996 ice thickness data (raised by Ref 1)*
- *C4: clarification on how grounding line movement and associated loss of basal traction is included in our experiments (raised by Ref 1 and 3)*
- *C5: aspects of eqn 2 (raised by Ref 2)*
- *C6: improved references to existing literature (raised by Ref 1)*

We have addressed C5 and C6 at length in previous replies to the reviewers, i.e. we decided to remove eqn 2 and have expanded references to existing literature throughout the manuscript. Our replies to C1-4 are detailed below.

Editor: “Given the authors response to the reviews, it seems the minor and more substantial points are addressable by the authors or have already been addressed very well (see track change document) and the manuscript will likely get into a state to be accepted for publication.

Based on the response there are, however, a few points where the authors have not undertaken revisions or the authors disagree to the referees, and in the response they have given a convincing and detailed explanations or justifications to their decision, which is fine. However, in my view these answers (or parts thereof) may also be relevant for the general reader of the manuscript and not just the referees, and some explicit but very brief additional explanations/justifications (or links to the supplements) in the main text may be helpful. For example, a lengthy explanation has been given to the referees on the point of the joined optimization of A and C, but it is not clear/explicit if any of these explanations are planned to be incorporated into the manuscript. These explanations/justifications/clarifications should not just go to the referees, but some aspects of it may well be interesting for the general reader and should perhaps be considered in the main text. Specifically, for the case of the joined A and C optimization (Ref 1 and 3), some additional figures and clarifying text have been added in the supplement B2 which is helpful, but I think in the main text an additional reference to these add-ons in the supplements and maybe a brief discussion in the main text clarifying this point would be useful.”

In reply to C1 and C2: we have made a number of changes to motivate and better explain our choice of optimization scheme and optimization parameters. In particular, lines 205-208 (refers to the tracked changes at the end of this document) now include a word of caution about the solutions for A and C, and we explicitly refer to appendices B and D for a detailed discussion about the choice of optimization parameters and robustness of our results with respect to this choice. In turn, we have expanded Appendix B to highlight the role of the regularization multipliers (lines 535-546) including our motivation to invert for A and C across the full domain. We have also added some further context to our choice of prior information for A in lines 547-558.

Editor: “To Ref1 comment 1: quality RS-data: a new figure has been added in the supplement, but in the main text, a reference to this figure and a short comment to it would be useful (relative dh change accurate).”

In reply to C3: we have rewritten this part of the methods, see lines 145-171. We highlight our use of elevation changes (rather than a snapshot DEM) to estimate the ice thickness in 1996, and point out that this new approach is more accurate. We now refer the reader to the newly added figure A1 in the main manuscript, both in the context of the dh/dt data coverage (lines 161-165) and the good agreement between model and DInSAR grounding line locations in 1996 (line 167-169).

Editor: “To Ref1 comment to line 139: data coverage: refer to this fig. A1 also in the main text.”
See previous reply.

Editor: “clarification of interaction of grounding line and thinning in optimization”

In reply to C4: Throughout the manuscript we have clarified that the ‘thinning’ experiment (described lines 229-231) includes grounding line movement and therefore implies the loss of traction in newly ungrounded areas. We refer to lines 76-77, 215-216, 239-241, 264-265 and 303 in the manuscript with tracked changes, as well as the caption of Fig. 3.

Editor: “To Ref1 comment to line 451 and similar Ref3 (robustness of inversion results): the essence of this response would probably also be relevant for the general reader (not just referee) and could be briefly included in the main manuscript.”

In reply to C2: We prefer to keep details and discussions about the model configuration and optimization procedure in one place, and have therefore expanded Appendix B instead of the main manuscript. We have commented on the robustness of our results with respect to the choice of a priori values for A (lines 549-551) and have better motivated our choice of spatially constant regularization pre-multipliers (lines 541-546) and a priori values for A (lines 551-554). We comment that our results are robust across a range of pre-multiplier and a priori values, and refer to Appendix D

for a detailed discussion about the dependency on γ_s , which multiplies the gradient term in the regularization.

Editor: “For the ease of reference to the author response by the editor it maybe useful to perhaps number the responses the major referee comments (e.g. R1.3....).”

By numbering the main reviewer comments by C1-6 (see above) we hope to have addressed this suggestions by the editor.

Drivers of Pine Island Glacier ~~retreat from~~ speed-up between 1996 ~~to and~~ 2016

Jan De Rydt¹, Ronja Reese², Fernando S Paolo³, and G. Hilmar Gudmundsson¹

¹Department of Geography and Environmental Sciences, Northumbria University, Newcastle upon Tyne, UK

²Potsdam Institute for Climate Impact Research (PIK), Member of the Leibniz Association, Potsdam, Germany

³Jet Propulsion Laboratory, California Institute of Technology, Pasadena, CA, USA

Correspondence: Jan De Rydt (jan.rydt@northumbria.ac.uk)

Abstract. Pine Island Glacier in West Antarctica is among the fastest changing glaciers worldwide. Over the last two decades, the glacier has lost in excess of a trillion tons of ice, or the equivalent of 3 mm of sea level rise. The ongoing changes are ~~commonly attributed to~~ thought to have been triggered by ocean-induced thinning of its floating ice shelf, grounding line retreat and the associated reduction in buttressing forces. However, other drivers of change such as large-scale calving, changes in ice rheology and basal slipperiness could play a vital, yet unquantified, role in controlling the ongoing and future evolution of the glacier. In addition, recent studies have shown that mechanical properties of the bed are key to explaining the observed speed-up. Here we used a combination of the latest remote sensing datasets between 1996 and 2016, data assimilation tools and numerical perturbation experiments to quantify the relative importance of all processes in driving the recent changes in Pine Island Glacier dynamics. We show that (1) calving and ice shelf thinning have caused a comparable reduction in ice-shelf buttressing over the past two decades, that (2) simulated changes in ice flow over a viscously deforming bed are only compatible with observations if large and widespread changes in ice viscosity and/or basal slipperiness are taken into account, and that (3) a spatially varying, predominantly plastic bed rheology can closely reproduce observed changes in flow without marked variations in ice-internal and basal properties. Our results demonstrate that in addition to its evolving ice thickness, calving processes and a heterogeneous bed rheology play a key role in the contemporary evolution of Pine Island Glacier.

15 *Copyright statement.* ©2020. This work is distributed under the Creative Commons Attribution 4.0 License.

1 Introduction and motivation

Since the 1990s, satellite measurements have comprehensively documented the sustained acceleration in ice discharge across the grounding line of Pine Island Glacier (PIG, Fig. 1) in West Antarctica (Rignot et al., 2002; Rignot, 2008; Rignot et al., 2011; Mouginot et al., 2014; Gardner et al., 2018; Mouginot et al., 2019b). The changes in flow speed are an observable manifestation of the glacier's dynamic response to both measurable perturbations, such as calving and ice shelf thinning, and poorly constrained variations in physical ice properties and basal sliding. Evidence from indirect observations have indicated that changes in ice shelf thickness have occurred since at least some decades before the 1970s (Jenkins et al., 2010; Smith

et al., 2017; Shepherd et al., 2004; Pritchard et al., 2012). Within the last two decades, thinning of the grounded ice (Shepherd et al., 2001; Pritchard et al., 2009; Bamber and Dawson, 2020), intermittent retreat of the grounding line (Rignot et al., 2014), changes in calving front position (Arndt et al., 2018) and the partial loss of ice shelf integrity (Alley et al., 2019) have all been reported in considerable detail. At the same time, numerical simulations of ice flow have confirmed the strong link between ice-shelf thinning, which reduces the buttressing forces, and the increased discharge across the grounding line (~~Schmeltz et al., 2002; Payne et al., 2004; Favier et al., 2014; Arthern and Williams, 2017; Reese et al., 2018; Gudmundsson et al., 2019~~) (Schmeltz et al., 2002; Payne et al., 2004; Joughin et al., 2010; Seroussi et al., 2014; Favier et al., 2014; Arthern and Williams, 2017; Reese et al., 2019).

. Due to the dynamic connection between ocean-driven ice shelf melt rates and tropical climate variability (Steig et al., 2012; Dutrieux et al., 2014; Jenkins et al., 2016; Paolo et al., 2018), several model studies have ~~primarily~~ focused on the important problem of simulating the response of PIG to a potential anthropogenic intensification of melt. Such external perturbations, in combination with ice-internal feedbacks including the Marine Ice Sheet Instability, can force PIG along an unstable and potentially irreversible trajectory of mass loss (Favier et al., 2014; Rosier et al., 2020). Whereas significant progress has been made in simulating the melt-driven retreat of PIG, less attention has been given to other processes that could affect the force balance and thereby inhibit or foster changes in ice dynamics. Increased damage in the shear margins of the ice shelf, for example, has been reported by Alley et al. (2019) and Lhermitte et al. (2020), and is known to reduce the buttressing capacity of an ice shelf (Sun et al., 2017). Moreover, a series of recent calving events has ~~caused~~led to a sizeable reduction in the extent of the ice shelf, and caused a potential loss of contact with pinning points along the eastern shear margin (Arndt et al., 2018).

The relative impact of changes in ice geometry, basal shear stress and/or ice rheology on the dynamics of PIG has previously been emphasised in numerical studies by e.g. Schmeltz et al. (2002); Payne et al. (2004); Gillet-Chaulet et al. (2016); Joughin et al. (2019) and Brondex et al. (2019). In all cases, some combination of thickness changes, ice softening, a reduction in ice shelf buttressing or variations in basal shear stress were required to attain an increase in flow speed comparable to observations. Similar conclusions were reached for other Antarctic glaciers. Based on a comprehensive series of model perturbation experiments, Vieli et al. (2007) suggested that the acceleration of the Larsen B Ice Shelf prior to its collapse in 2002 could not solely be explained by the retreat of the ice shelf front or ice shelf thinning, but required a further significant weakening of the shear margins. Complementary conclusions were reached by Khazendar et al. (2007), who demonstrated the important interdependence of the calving front geometry, a variable ice rheology and flow acceleration based on data assimilation and model experiments for the Larsen B Ice Shelf.

In order to comprehensively diagnose the importance of all processes that have contributed to the acceleration of PIG ~~between years over the period~~ between years over the period 1996 ~~and to~~ and to 2016, this study brings together the latest observations and modelling techniques. We consider how calving, ice shelf thinning, the induced dynamic thinning upstream of the grounding line and potential changes in ice-internal and basal properties have caused a different dynamic response across the ice shelf, the glacier's main trunk, the margins and tributaries. Initial observations indicated that the speed-up of PIG was primarily confined to its fast-flowing central trunk (Rignot et al., 2002; Rignot, 2008), though more complex, spatiotemporal patterns of change have emerged more recently (Bamber and Dawson, 2020). The rapid and spatially diverse acceleration of the flow is an expression of the glacier's dynamic response to changes in the force balance, and it is imperative that numerical ice flow models are capable of

reproducing this complex behavior in response to the correct forcing. In general, the driving stress (τ_d), which depends on the ice thickness distribution, is balanced by resistive stresses that include the basal drag (τ_b), side drag through horizontal shear (τ_W), longitudinal resistive forces (τ_L) and back forces by the ice shelf (τ_{IS}):

$$\tau_d = \tau_b + \tau_W + \tau_L + \tau_{IS}. \quad (1)$$

It is conceivable that each of the terms in Eq. 1 has changed considerably in recent decades, whilst maintaining a balance at all times. This in response to changes in calving front position, ice thickness, ice properties and/or basal slipperiness. The interplay between different changing forces, in combination with the appropriate boundary conditions, underlie the observed dynamical changes of PIG, and form the backbone of any numerical model simulation. In response to changes in the stress balance, modeled changes in ice velocity between time t_0 and t_1 can be expanded as follows:-

$$\Delta U(\mathbf{x}) \equiv U_{t_1}(\mathbf{x}) - U_{t_0}(\mathbf{x}) = \Delta U_{\text{Calv}} + \Delta U_{\text{Thin}} + \Delta U_A + \Delta U_C,$$

where terms on the right hand side indicate different contributions to the changes in ice flow, caused by variations in calving front position (ΔU_{Calv}), changes in ice thickness (ΔU_{Thin}), changes in ice properties commonly parameterized by a rate factor A speed-up of PIG (ΔU_A), and changes in basal slipperiness C (ΔU_C). Note that these contributions are not generally independent due to feedbacks within the system, and that only the total sum, ΔU , can be observed directly. The velocity component related to changes in ice thickness, ΔU_{Thin} , generally consists of two contributions: an instantaneous response due to ice shelf thinning, as investigated by e.g. Gudmundsson et al. (2019), and the ΔU . Present-day observations of ΔU are generally assumed to be dominated by ice shelf thinning and induced dynamic loss and redistribution of mass upstream of the grounding line. We will separately assess the impact of both components. Present-day observations of ΔU are generally assumed to be dominated by ΔU_{Thin} , whereas other contributions, which includes grounding line retreat and the associated loss of basal traction. Other possible contributions to ΔU , such as ice front retreat or changes in ice viscosity (including damage) or basal slipperiness, remain unquantified and are not generally included in model simulations of future ice flow at decadal to centennial timescales. In particular, temporal changes in ice viscosity and basal sliding are ignored such that $\Delta U_A + \Delta U_C = 0$, whereas only a minority of ice flow models include (simple) parameterizations of calving. These missing processes, if important, could lead to a systematic bias in model projections of future ice loss, or could prompt the use of unrealistically large perturbations in, e.g., τ_{IS} in an attempt to reproduce observed values of ΔU .

In this study we used a regional configuration of the shallow ice stream flow model, \dot{U}_a (Gudmundsson, 2020), for PIG to estimate the individual components of diagnose how individual processes (calving, ice thinning and associated grounding line movement, changes in ice viscosity and basal slipperiness) have contributed to ΔU in Eq. ?? between $t_0 = 1996$ and $t_1 = 2016$. Results enabled us to quantify the relative importance of each driver of change for the contemporary evolution of PIG, and validate the ability of current-generation ice flow models to reproduce the complex response of PIG to a range of realistic forcings. It is important to note that results were *not* derived from transient simulations of glacier flow based on (uncertain) estimates of the initial model state and external forcings. Instead, the over the period 1996 to 2016. The diagnostic model response to a series of prescribed changes in ice geometry was analysed, based on the latest observations of calving

and ice thinning rates and calving between 1996 and 2016. For each perturbation, changes in the stress balance (Eq. 1) and the associated ice flow response (ΔU_{Calv} and ΔU_{Thin}) were computed. Assuming closure of the velocity budget in Eq. ?? and observed values for ΔU , an estimate for $\Delta U_A + \Delta U_C$ was obtained. Knowledge about the magnitude and spatial distribution of each contribution in Eq. ?? allowed us to

95 Any further discrepancies between modeled and observed changes in velocity were attributed to variations in ice properties, commonly parameterized by a rate factor A , and changes in basal slipperiness C . Results enabled us to validate the ability of current-generation ice flow models to reproduce the complex response of PIG to a range of realistic forcings, and to verify whether common model assumptions such as $\Delta U_{\text{Calv}} = 0$ and $\Delta U_A + \Delta U_C = 0$ a static calving front and fixed ice viscosity and basal slipperiness are indeed justified, ~~at least for contemporary flow conditions.~~

Although the aforementioned method provides insights into the individual contribution of geometrical perturbations and

100 changes in ice viscosity and basal slipperiness to overall changes in ice flow, ~~the partitioning between different components of the ΔU budget likely depends~~ results will likely depend on a number of structural assumptions within the ice flow model. In particular, assumptions about the form of the basal sliding law are likely to precondition the partitioning of ΔU . Indeed, ~~previous model~~ Previous studies have shown that different forms of the sliding law, for example, can produce a distinctly different simulated response of PIG to changes in geometry (Joughin et al., 2010; Gillet-Chaulet et al., 2016; Joughin et al., 2019; Brondex et al.

105 ~~Based on the assumption that $\Delta U \approx \Delta U_{\text{Thin}}$, ice thickness~~ (Joughin et al., 2010; Gillet-Chaulet et al., 2016; Joughin et al., 2019; Brondex et al., 2019). Joughin et al. (2010) and Joughin et al. (2019) showed that a regularized Coulomb law or the plastic limit of a ~~Weertman non-linear viscous~~ power-law provide a better fit between modeled and observed changes in surface velocity along the central flowline of PIG, compared to a commonly used ~~viscous Weertman law~~ Weertman law with a cubic dependency of the sliding velocity on the basal shear stress. Motivated by the above considerations, we explore new ways to derive spatially variable constraints on the form of the sliding law, and thereby provide the first comprehensive, spatially distributed map of basal rheology beneath PIG.

The remainder of this paper is organised as follows. In Sect. 2.1 we introduce the observational datasets used to constrain and validate the ice flow model. Additional details about our data processing methods are provided in App. A. Section 2.2 outlines the experimental design, and provides a summary of the main model components. Further technical details about the

115 model setup and a discussion about the sensitivity of our results to numerical model details are provided in App. B and App. D respectively. Results and an accompanying discussion of all experiments is provided in Sect. 3.1-3.3. Final conclusions are formulated in Sect. 4.

2 Data and methods

The first aim of this study is to simulate the dynamic response of PIG to a series of well-defined geometric perturbations

120 ~~between years over the period~~ 1996 ~~and to~~ 2016, and compare model output to observed changes in surface speed over the same time period. As detailed in Sect. 1, geometric perturbations are considered to be observed changes in the calving front position and observed changes in ice thickness ~~For each perturbed geometry, a diagnostic solution for the surface velocities, denoted by U_* , was obtained, where the subscript $*$ refers to individual perturbations. Since we~~ of the ice shelf and grounded ice. We

are primarily interested in the relative contribution of each perturbation to the overall-observed speed-up of PIG between 1996 and 2016, our focus will be on relative changes $\Delta U_*/\Delta U$, where $\Delta U_* = U_* - U_{96}$ and $\Delta U = U_{16} - U_{96}$. In order to compute the relative changes in surface flow, two types of model experiment are required: (1) inverse simulations, which were used to obtain model configurations that are as close as possible to the observed state of PIG in 1996 (2016). Each contribution can be characterized by a relative change in velocity, $(U_{\text{pert}} - U_{96})/(U_{16} - U_{96})$, where U_{96} and 2016 (U_{16}), and (2) perturbation experiments to obtain estimates of U_* , starting from the 1996 model configuration. In and U_{16} were obtained from model optimization experiments, as described in Sect. 2.2.1, and velocities of the perturbed states (U_{pert}) were obtained from a series of diagnostic model calculations, as described in Sect. 2.1 we list 2.2.2. First, the data sources required for these experiments, whereas a detailed overview of the experimental design is provided in Sect. 2.2, each of these experiments are listed.

2.1 Observed changes of Pine Island Glacier between 1996 and 2016

Our study area and model domain encompasses the 135,000 km² grounded catchment (Rignot et al., 2011) and seaward floating extension of PIG in West Antarctica, as depicted in Fig. 1a. To investigate the physical processes that forced the contemporary speed-up of the glacier, and its increase in grounding line flux between years 1996 and 2016, we ~~required~~ needed detailed observations of the surface velocity, ice thickness and calving front position for both years.

The surface velocity measurements used in this study were taken from the MEaSUREs database (Mouginot et al., 2019a, b). For 1996, Synthetic Aperture Radar data from the ERS-1/2 mission were processed using interferometry techniques and combined into a mosaic with effective timestamp 01/01/1996. The MEaSUREs velocities for 2016 were based on feature tracking of Landsat 8 imagery with effective timestamp 01/01/2016. The change in surface speed between both years (~~denoted by $\Delta U = U_{16} - U_{96}$~~) is shown in Fig. 1b, and we refer to e.g. Rignot et al. (2014) and Gardner et al. (2018) for a more comprehensive description of these observations.

~~Recent estimates of ice thickness were obtained from the BedMachine Antarctica dataset (Morlighem et al., 2020), which provides both high-resolution surface topography~~ To obtain an accurate estimate of the ice thickness distribution of PIG in 1996, we compiled a time series of surface height changes from a comprehensive set of overlapping satellite altimeter data between 1996 and 2016. The integrated altimeter trend over the 20-year time interval, shown in Fig. 1c, was subtracted from the recent Bedmachine Antarctica reference thickness (Morlighem et al., 2020). As satellite altimeters are very precise instruments capable of detecting small changes in surface elevation, our approach is more robust compared to thickness estimates based on a snapshot Digital Elevation Model, such as the ERS-1 derived product (Bamber and Bindshadler, 1997), which has poor vertical accuracy. The Bedmachine Antarctica reference thickness is based on the ~~REMA mosaic (Howat et al., 2019) and improved estimates~~ high-resolution Reference Elevation Model of Antarctica (REMA, Howat et al. (2019)) tied to Cryosat-2 data, and an improved estimate of bedrock topography using mass conservation methods. The nominal date ~~for this dataset of the Bedmachine geometry~~ corresponds to the date stamp of the REMA elevation model, which is spatially variable but largely between 2014 and 2018 for PIG. ~~For consistency with previous notation we refer to the~~ We denote the 1996 and BedMachine Antarctica ice thickness estimates as H_{16} and we assume a uniform timestamp of 01/01/2016.

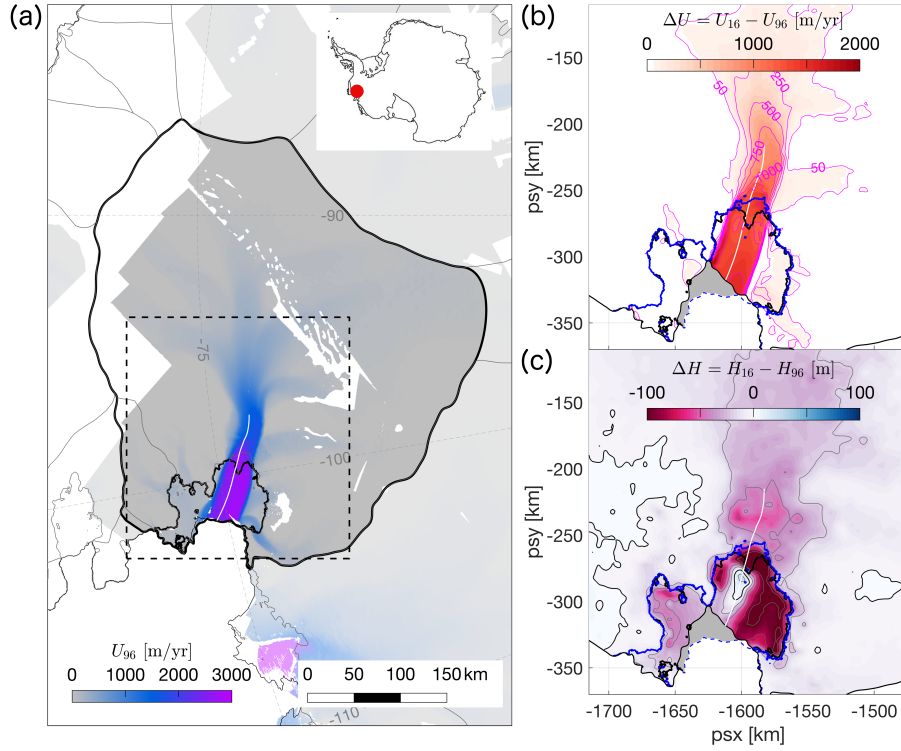


Figure 1. Pine Island Glacier (PIG) and its location in West Antarctica. **(a)** Surface speed of PIG in 1996 in m/yr, as reported by the MEaSUREs program (Mouginot et al., 2019a). Solid black outlines delineate the extent of the PIG catchment (Rignot et al., 2011) and 1996 grounding line position (Rignot et al., 2014). The white line along the central flowline indicates the location of the transect in Fig. 2. The dashed rectangle corresponds to the extent of panels **b** and **c**. **(b)** Observed increase in surface speed (Mouginot et al. (2019a), colours and contours in m/yr) and loss of ice shelf extent (grey shaded area) between 1996 and 2016. The blue line indicates the 2011 grounding line (Rignot et al., 2014). **(c)** Total change in ice thickness between 1996 and 2016 (ΔH in m), based on a combination of CPOM data (Shepherd et al., 2016) for the grounded ice and newly analyzed data for the ice shelf (Appendix A). The zero contour is shown in black, other contours in grey are spaced at 20 m intervals.

Ice thickness estimates for 1996, henceforth denoted by H_{96} , were obtained by subtracting measurements of ice thickness change between 1996 and 2016, denoted by ΔH , from and H_{16} , i.e. respectively, where $H_{96} = H_{16} - \Delta H$ with ΔH the integrated altimeter trend. Estimates of ΔH were based on a combination of existing CPOM measurements of thickness change rates (Shepherd et al., 2016) surface elevation changes for areas upstream of the 2016 grounding line, (Shepherd et al., 2016) and newly analyzed data for the floating ice shelf. Detailed information about the latter A detailed description of our methods and a map of the data coverage for ΔH can be found in App. A. The resulting values for ΔH , linearly interpolated across the grounding line and in data sparse areas, are shown in and Fig. 1c, and provide the most comprehensive observation-based ice shelf and grounded ice thickness changes for PIG to date A1 respectively.

165 The grounding line location for H_{16} (blue line in Fig. 1b-c) corresponds to the DInSAR derived grounding line in 2011 from Rignot et al. (2014), since this is included as a constraint in the generation of the BedMachine Antarctica bed topography. ~~In addition, (Morlighem et al., 2020). The grounding line for $H_{96} = H_{16} - \Delta H$ approximately follows the 1992-1996 DInSAR estimates (Rignot et al., 2014), as shown in Fig. A1. To further improve the agreement between the model and DInSAR grounding line in 1996, some~~ localized adjustments less than 150 m were made to the bed topography ~~to ensure that the grounding line-. The final grounding line location for H_{96} (black lines is depicted in Fig. 1a-c) corresponds to the DInSAR-derived grounding line in 1992-1996 (Rignot et al., 2014).~~

Alongside the above-listed observed changes in flow dynamics and ice thickness, the calving front of PIG retreated by up to 30 km between 1996 and 2016 during a succession of large-scale calving events; see e.g. Arndt et al. (2018). We traced the calving front positions in 1996 and 2016 from cloud free Landsat 5 and Landsat 8 panchromatic band images with timestamps 18/02/1997 and 25/12/2016 respectively. Both outlines are included in Fig. 1b-c, and the ice shelf area that was lost between 1996 and 2016 is shaded in grey.

2.2 Experimental design

~~We discuss the numerical experiments required to-~~

2.2.1 Optimization experiments

180 To obtain an optimal model configuration for the state of PIG in 1996 (U_{96}) and 2016 (U_{16}) in Sect. 2.2.1. ~~Experiments that provide estimates of U_* for a series of observed perturbations in the geometry of PIG are introduced in Sect. 2.2.2. Experiments that simulate changes in the rate factor or basal slipperiness are detailed in Sect. 2.2.3.~~

2.2.2 ~~Inverse experiments~~

~~We, we~~ explicitly solved the stress balance ~~in year 1996 (an analogous routine was applied for 2016)~~ by assimilating the ~~known-estimated~~ ice thickness (H_{96}), calving front position and ~~surface velocity (U_{96})~~ measured surface velocities in the shallow ice stream (SSA) model \dot{U}_a (Gudmundsson et al., 2012; Gudmundsson, 2020). An analogous routine was applied for 2016. This ‘data assimilation’ or ‘inverse optimization’ step is commonly adopted in glaciology (see MacAyeal (1992) for one of the earliest examples) to minimize the misfit between modeled and observed surface velocities through the optimization of uncertain physical parameters. The inverse optimization capabilities of \dot{U}_a (further details are provided in App. B) were used 190 to optimize the uncertain spatial distribution of the rate factor, A , and basal slipperiness, C . These physical parameters define the constitutive model and the relationship between basal shear stress τ_b and basal sliding velocity U_b respectively:

$$\dot{\epsilon} = A \tau_E^{n-1} \tau, \quad (2)$$

$$\tau_b = C^{-1/m} \|U_b\|^{\frac{1}{m}-1} U_b \quad (3)$$

Glen’s law, Eq. 2, relates the strain rates $\dot{\epsilon}$ to the deviatoric stress tensor τ . A creep exponent $n = 3$ was used throughout this 195 study. Equation 3 is known as a Weertman sliding law (Weertman, 1957), and describes a linear ~~viscous, non-linear~~ viscous

or close-to plastic bed rheology for $m = 1$, $m > 1$ and $m \gg 1$ respectively. Throughout this study, a range of values for m are considered, as specified below. For each m we performed a new inversion for A and C , which caused small variations in τ_b between cases, but produced an optimal fit between modeled and observed surface velocities in each case. This method differs from other studies, e.g. Joughin et al. (2019), who performed a single inversion for $m = 1$, and obtained C for different values of m by solving Eq. 3 under the assumption that τ_b remains constant. We consider our approach to be more appropriate for this study, as our focus is primarily on an accurate model representation of the surface flow (e.g. Eq. ??). Results for A and C for example results for $m = 3$ are provided in Appendix App. B. The outcome of the inverse step is a best estimate for each term optimization step is an estimate for A and C that best fits the stress balance in Eq. 1, based on for given observations of geometry and surface velocity of PIG in year 1996. Analogous results were obtained for 2016, associated measurement errors and assumptions about the prior values of A and C . Solutions for A and C are not generally unique, but depend on the choice of optimization scheme and several poorly constrained optimization parameters. Further details about the used optimization scheme and a discussion about the robustness of our results with respect to uncertain optimization parameters are provided in App. B and D.

2.2.2 Geometric perturbation experiments

In the second step we carried out The optimal model configuration in 1996 was subsequently used as the reference state for a series of numerical perturbation experiments, starting from the 1996 model configuration, to simulate the aimed at simulating the impact of observed changes in geometry on the flow of PIG. The rate factor and basal slipperiness were kept fixed to their 1996 values. For each perturbation, the modified force balance (Eq. 1) and corresponding surface velocities, U_* , perturbed velocities were diagnosed within \dot{U}_a . Experiments are The rate factor and basal slipperiness were kept fixed to their 1996 values, although the basal traction was reduced to zero and slipperiness values became irrelevant in areas that ungrounded due to ice thinning. Experiments will be referred to as \mathcal{E}_*^m with a variable subscript to indicate the type of perturbation and a superscript to specify the value of the sliding exponent m . Experiments were carried out for a range of exponents so we leave m unspecified for now.

- $\mathcal{E}_{\text{Calv}}^m$. Changes in the calving front location were prescribed to reflect the loss of ice shelf between 1996 and 2016 (see Fig. 1b-c). All model grid elements downstream of the 2016 calving front (grey shaded area in Fig. 1b) were deactivated, whilst elements upstream of the 2016 calving front remained fixed to avoid numerical interpolation errors. All other model variables were kept fixed. The difference between the 1996 surface velocity and the perturbed velocity will be denoted by $\Delta U_{\text{Calv}} = U_{\text{Calv}} - U_{96}$.
- $\mathcal{E}_{\text{ISThin}}^m$. Changes in ice shelf thickness were prescribed, corresponding to observed thinning of the ice shelf between 1996 and 2016 (Fig. 1c). Note that the calving front and grounding line location did not change in this experiment. This experiment, which is similar to previous studies, by e.g. (Reese et al., 2018; Gudmundsson et al., 2019). Reese et al. (2018) and Gudmundsson et al. (2019). The instantaneous change in surface velocity due to ice shelf thinning will be denoted by $\Delta U_{\text{ISThin}} = U_{\text{ISThin}} - U_{96}$.

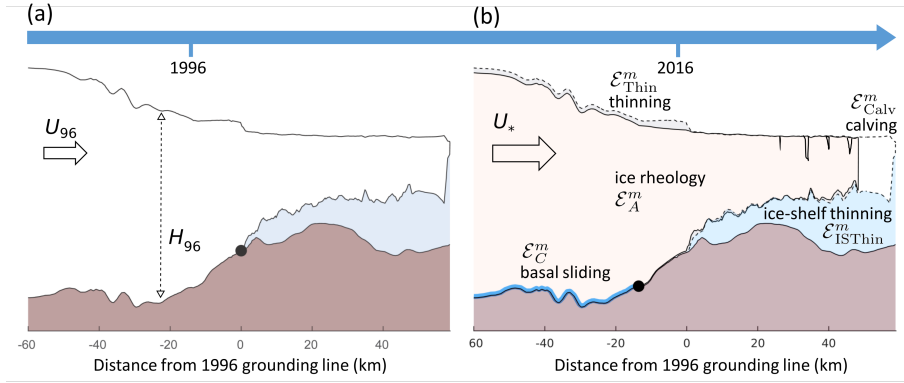


Figure 2. Overview of changes along the Pine Island Glacier centerline from (a) year 1996 to (b) year 2016. Increased ice flow is driven by a combination of calving, ice-shelf thinning and dynamic thinning with movement of the grounding line, as well as changes in basal sliding and ice rheology. Transects of the geometry are based on observations along the flowline indicated in Fig. 1; black dots indicate the respective grounding line positions in both years. Crevasses are introduced for illustration purposes only and do not strictly correspond to observed features. The importance of each ‘driver of change’ was investigated in a series of numerical perturbation experiments, denoted by \mathcal{E}_*^m in panel b, with m indicating the sliding exponent and $*$ the respective experiment described in section 2.2.

- $\mathcal{E}_{\text{Thin}}^m$. Observed changes in both the floating and grounded parts of PIG were prescribed. This caused the grounding line to move from its 1996 position (black line in Fig. 1b-c) to the 2016 position (blue line in Fig. 1b-c). Velocity changes caused by thinning of the floating and grounded ice will be denoted by $\Delta U_{\text{Thin}} = U_{\text{Thin}} - U_{96}$.
- $\mathcal{E}_{\text{CalvThin}}^m$. Combined changes in calving front position (as in $\mathcal{E}_{\text{Calv}}^m$), and thinning (as in $\mathcal{E}_{\text{Thin}}^m$) were prescribed. Corresponding velocity changes will be denoted by $\Delta U_{\text{CalvThin}} = U_{\text{CalvThin}} - U_{96}$.

A schematic overview of the experiments is provided in Fig. 2. While $\mathcal{E}_{\text{Calv}}^m$ allows us to assess the time-integrated instantaneous impact of calving between 1996 and 2016 (ΔU_{Calv}), and, the experiment $\mathcal{E}_{\text{ISThin}}^m$ simulates the instantaneous response to total changes in ice shelf thickness between 1996 and 2016 (ΔU_{ISThin}), both experiments ignore the time-dependent, dynamic response of the upstream grounded ice. These 2016. The separate perturbations make it possible to disentangle the changes in ice shelf buttressing caused by each process, and hence their relative importance for driving the transient evolution of the flow. However, both experiments ignore the time-dependent, dynamic response of the upstream grounded ice and the associated loss of basal traction due to grounding line movement. Dynamic thinning of grounded ice, as well as migration of the grounding line, is included in the experiments $\mathcal{E}_{\text{Thin}}^m$, which allows us to determine the full dynamic response to changes in ice thickness (ΔU_{Thin}). Finally, the experiment $\mathcal{E}_{\text{CalvThin}}^m$ combines both calving and ice thinning, and thereby accounts for all geometric perturbation, and provides a spatial distribution of $\Delta U_{\text{Thin}} + U_{\text{Calv}}$ perturbations.

2.2.3 Estimates of changes in A and C

Later on we show that geometric perturbations alone are not able to fully reproduce the observed patterns of speed-up across the PIG catchment, i. e. $\Delta U \neq \Delta U_{\text{CalvThin}}$. It is conceivable that, along with the evolving geometry, variations in ice and basal properties have contributed to the changes in flow between 1996 and 2016, i. e. $\Delta U_A + \Delta U_C \neq 0$. Indeed, feedback mechanisms are likely to cause an important interdependence between geometry-induced changes in ice flow, shear softening and/or changes in basal shear stress. Reliable observations of changes in rheology and basal properties are not available, but numerical inverse optimization simulations can provide valuable insights into their evolution. We used the inverse method as described in Sect. 2.2.1 and App. B to estimate necessary bounds on the magnitude and spatial distribution of changes in A and C that are required beside the geometrical changes already applied, to produce the speed-up of PIG between 1996 and 2016. Changes in A and C are treated separately.

- \mathcal{E}_A^m . The aim of this experiment is to determine possible changes in the rate factor between 1996 (A_{96}) and 2016 (A_{16}). A_{96} was previously obtained in part 1 (inverse optimization step) of the experimental design. To estimate A_{16} , an inverse optimization problem was solved for the 2016 PIG geometry (H_{16}) and velocities (U_{16}), but using a cost function that was minimized with respect to A only. The slipperiness C was kept fixed to its 1996 solution.
- \mathcal{E}_C^m . This experiment is analogous to \mathcal{E}_A^m , but the cost function in the inverse problem was optimized with respect to C only, whereas the rate factor A was kept fixed to its 1996 solution.

3 Results and discussion

3.1 Ice dynamics response to changes in geometry between 1996 and 2016

We present results for the first set of perturbation experiments, which simulate the impact of observed changes in geometry on the flow of PIG. As detailed in section Sect. 2.2.2, perturbations are split between four separate cases: 1) calving ($\mathcal{E}_{\text{Calv}}^3$), 2) thinning of the ice shelf ($\mathcal{E}_{\text{ISThin}}^3$), 3) thinning of the ice shelf and grounded ice ($\mathcal{E}_{\text{Thin}}^3$), and which includes associated movement of the grounding line and changes in basal traction, and 4) the combined impact of all observed geometrical changes the above ($\mathcal{E}_{\text{CalvThin}}^3$). We did not previously specify the value of the sliding exponent, however, here we set $m = 3$, which is a commonly adopted value in ice flow modeling and describes a viscous, rate-strengthening non-linear viscous (or Weertman) bed rheology. We will explore results Results for different values of m will be explored in Sect. 3.3.

Results for the relative change in surface speed, $(U_{\text{pert}} - U_{96}) / (U_{16} - U_{96})$, for each of the above perturbations are presented in Fig. 3a-d. In addition to spatial maps of relative velocity changes, we present flux calculations for two gates perpendicular to the flow within the central part of PIG, as displayed in Fig. 3a. Gate 1 is situated about 50 km upstream of the 2016 grounding line and captures the inland propagation of changes in ice flow. Gate 2 approximately coincides with the 2016 grounding line position and captures changes in grounding line flux, which is a direct measure for PIG's increasing contribution to sea level rise, and an important indicator of change.

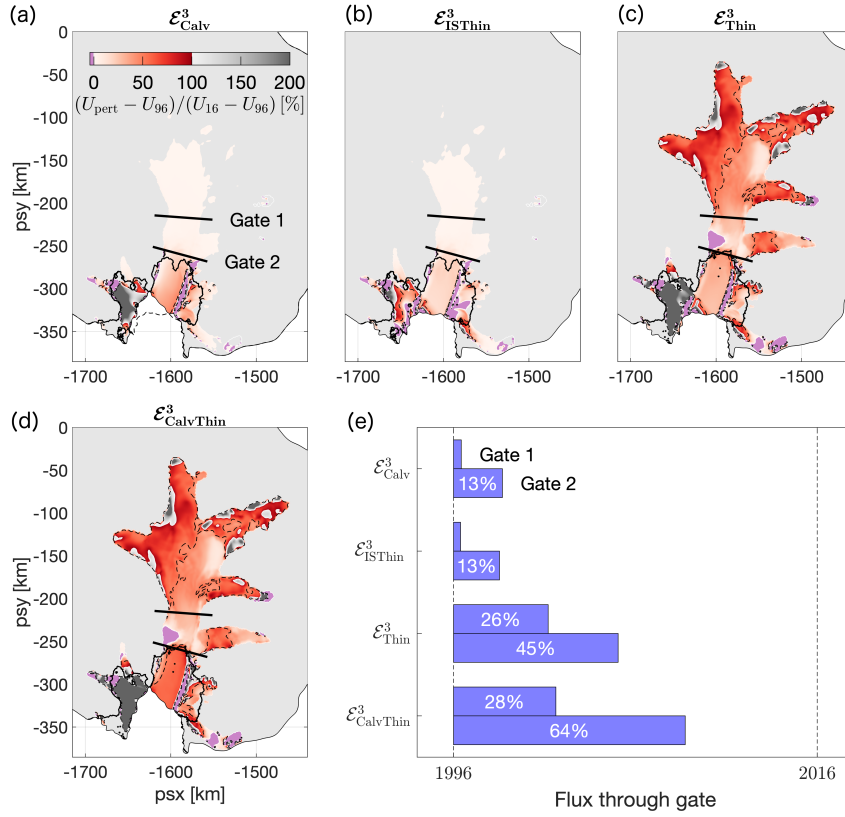


Figure 3. Modelled changes in surface speed compared to 1996 for prescribed perturbations of the Pine Island Glacier geometry. (a) Retreat of the calving front, (b) thinning of the ice shelf, (c) thinning of the ice shelf and grounded ice, including grounding line retreat, (d) calving and thinning combined. For each perturbation, the modeled change in speed $(U_{\text{pert}} - U_{96}) / (U_{16} - U_{96})$ is expressed as a percentage of the observed speed-up between 1996 and 2016 $(U_{16} - U_{96})$. Dashed black lines correspond to the 50% contour. Panel (e) shows the percentage of the observed flux changes through Gate 1 and 2 that can be explained by the respective perturbations. The simulated impact of calving and thinning in experiment $\mathcal{E}_{\text{CalvThin}}^3$ ~~underestimates measured flux changes by 72%~~ only represent 28% and 36% of the measured flux changes respectively. Possible explanations for the unexplained increase in flow speed are provided in Sect. 3.2 and Sect. 3.3 .

275 Calving as simulated in $\mathcal{E}_{\text{Calv}}^3$ causes changes in flow speed that are predominantly restricted to the outer ice shelf, where it accounts for up to 50% of the observed speed-up between 1996 and 2016 (Fig. 3a). A smaller dynamical impact is also felt upstream of the grounding line, caused by the calving-induced reduction in ice shelf buttressing and mechanical coupling between the floating and grounded ice. Along the central, fast-flowing trunk of PIG, calving typically accounts for less than 10% of the observed speed-up, with little or no effect on the dynamics of the upstream tributaries. Our results are consistent

280 with earlier work by Schmeltz et al. (2002), in particular their calving scenario “part 2”. The only area with negative relative changes in our simulation is the western shear margin of the ice shelf, where modeled and observed changes in flow speed have the opposite sign. Extensive damage, a process that is not captured by this experiment, has caused this margin to migrate and

significant interannual variations in flow speed have been reported by Christianson et al. (2016), ~~a process that is not captured by this experiment.~~

285 Flux gates provide an alternative, aggregated way to convey the above results. We present flux calculations for two gates perpendicular to the flow within the central part of PIG, as displayed in Fig. 3a. Gate 1 is situated about 50 upstream of the 2016 grounding line and captures the inland propagation of changes in ice flow. Gate 2 approximately coincides with the 2016 grounding line position and captures changes in grounding line flux, which is a direct measure for PIG's increasing contribution to sea level rise, and an important indicator of change. Figure 3e shows that calving accounts for 2% and 13% of the observed
290 flux changes through Gate 1 and 2 respectively. ~~This supports the earlier conclusion that the retreat of the PIG calving front between 1996 and 2016 has caused only~~, which confirm the minor instantaneous changes to the flow upstream of the grounding line.

Thinning of the ice shelf as simulated in experiment $\mathcal{E}_{\text{Thin}}^3$ ~~$\mathcal{E}_{\text{ISThin}}^3$~~ induces a flow response that is similar to calving, as shown in Fig. 3b, and indicates that calving and ice shelf thinning have caused a similar comparable perturbation in the buttressing
295 forces. The largest percentage changes are found on the ice shelf, and are typically less than 25%, while the relative flux changes through Gate 1 and 2 are identical to the calving experiment (Fig. 3e). Ice shelf thinning is generally accepted to be the main driver of ongoing mass loss of PIG, and patterns of ice shelf thinning elsewhere in Antarctica are strongly correlated to observed changes in grounding line flux (Reese et al., 2018; Gudmundsson et al., 2019). However, the force perturbations that result from ice shelf thinning alone, in particular the instantaneous reduction in back forces τ_{IS} , are not sufficient to explain the magnitude
300 of observed changes in upstream flow, consistent with previous studies (Seroussi et al., 2014; Joughin et al., 2010, 2019). Indeed, experiment $\mathcal{E}_{\text{ISThin}}^3$ demonstrates that the direct and instantaneous contribution of ice shelf thinning to observed changes in grounding line flux are less than 25%. Instead, time-evolving changes in geometry and mass redistribution upstream of the grounding line, which may cause grounding line retreat and associated loss of basal traction, play a significant role in increasing the dynamic response of the glacier. These dynamic changes, caused indirectly by changes in the calving front position and
305 ice shelf thinning, were not captured by the experiments $\mathcal{E}_{\text{Calv}}^3$ and $\mathcal{E}_{\text{ISThin}}^3$, but are considered in experiment $\mathcal{E}_{\text{Thin}}^3$.

In experiment $\mathcal{E}_{\text{Thin}}^3$ we prescribed the time integrated change in ice thickness between 1996 and 2016 for both the floating ice shelf and upstream grounded ice. This perturbation incorporates the observed recession of the PIG grounding line between 1996 and 2016. The combined reduction in ice shelf buttressing, loss of basal friction due to grounding line retreat and changes in driving stress caused a significant and far-reaching impact on the flow, as displayed in Fig. 3c. Modeled changes on the
310 ice shelf are consistent with and similar in amplitude to $\mathcal{E}_{\text{ISThin}}^3$. Upstream of the grounding line, modeled changes relative to observations are between 25% and 50% along the central trunk and up to 100% along the tributaries. In addition, results demonstrate that glacier-wide changes in ice thickness account for 26% and 45% of the observed changes in ice flux through Gate 1 and 2 respectively (Fig. 3e).

In the final perturbation experiment, $\mathcal{E}_{\text{CalvThin}}^3$, the combined effect of calving and changes in ice thickness were simulated.
315 Modeled versus observed changes in surface speed are shown in Fig. 3d. The spatial pattern is consistent with previous experiments, and the amplitude of the response is approximately equal to the added response of experiments $\mathcal{E}_{\text{Calv}}^3$ and $\mathcal{E}_{\text{Thin}}^3$, i.e. $\Delta U_{\text{CalvThin}} \approx \Delta U_{\text{Calv}} + \Delta U_{\text{Thin}}$. The corresponding percentage changes in ice flux through Gate 1 and 2 are 28% and 64%

respectively, whereas modeled changes in flow across the ~~grounding-line-proper~~ actual grounding line account for about 75% of the observed increase in flux between years 1996 and 2016. Although this experiment prescribes all observed changes in
 320 PIG geometry over the observational period, model simulations are unable to capture a significant percentage of the observed speed-up. This is most noticeable along the fast-flowing central trunk upstream of the grounding line, whereas discrepancies decrease along the slow-flowing tributaries in the high catchment. We also note that in one area between Gate 1 and 2, modeled and observed changes in surface speed have opposite signs.

Although it is not unexpected to find differences between diagnostic model output and observations, the consistently sup-
 325 pressed response of the model to realistic perturbations in ice geometry is indicative of a structural shortcoming within our experimental design. Indeed, results show that for a non-linear viscous bed rheology described by a Weertman sliding law with constant sliding coefficient $m = 3$, changes in ice geometry alone cannot explain the complex and spatially variable pattern of speed-up over the observational period, i.e. $\Delta U \neq \Delta U_{\text{CalvThin}} U_{16} - U_{96} \neq \Delta U_{\text{CalvThin}}$. In the remainder of this study, two possible hypotheses are analyzed that enable to close the gap between geometry-induced changes in ice flow and the observed
 330 speed-up of PIG. The first ~~hypotheses~~ hypothesis, which is considered in ~~section~~ Sect. 3.2, assumes that bed deformation can indeed be described by a non-linear viscous power law with $m = 3$, but further temporal variations in ice viscosity and/or basal slipperiness are required in addition to changes in geometry: $\Delta U = \Delta U_{\text{CalvThin}} + \Delta U_A + \Delta U_C U_{16} - U_{96} = \Delta U_{\text{CalvThin}} + \Delta U_A + \Delta U_C$. The second, alternative hypotheses, discussed in ~~section~~ Sect. 3.3, assumes that internal properties of the ice and bed have not significantly changed between years 1996 and 2016, i.e. $\Delta U_A + \Delta U_C \approx 0$ $\Delta U_A \approx 0$ and $\Delta U_C \approx 0$, but a different physical
 335 description of the basal rheology is required instead.

3.2 Changes in the rate factor and basal slipperiness between years 1996 and 2016

In transient model simulations of large ice masses such as Antarctica's glaciers and ice streams, it is common to assume that the advection of A with the ice, or changes due to temperature variations and fracture as well as changes in basal slipperiness C , exert a second-order control on changes in ice flow. As such, temporal variability in A and C are often ignored, based on
 340 the assumption that these changes are sufficiently slow and do not significantly affect the flow on typical decadal to centennial timescales under consideration. The aim of experiments \mathcal{E}_A^3 and \mathcal{E}_C^3 , as outlined in section 2.2.3, is to establish whether this is a valid assumption, or whether previously ignored changes in A and/or C can provide a realistic explanation for the discrepancy between simulated and observed changes in the surface speed of PIG in the geometric experiment $\mathcal{E}_{\text{CalvThin}}^3$. Experiment \mathcal{E}_A^3 assumes that, in addition to changes in geometry, temporal variations in A alone are able to explain the significant ~~increases~~
 345 increase in flux that were unaccounted for in previous experiments. Alternatively, \mathcal{E}_C^3 assumes that, in addition to changes in geometry, temporal variations in C alone are able to explain the discrepancy in section 3.1 between the modeled and observed speed-up. In line with previous experiments we assume a Weertman sliding law with $m = 3$. The results for both experiments are summarized in Fig. 4.

Changes in A (Fig. 4a), needed to fully reproduce the speed-up of PIG between years 1996 and 2016, are spatially co-
 350 herent and predominantly positive. This suggests a reduction in ice viscosity between 1996 and 2016, either as a result of localized heating, enhanced damage within the ice column or changes in anisotropy. The largest changes are found in distinct

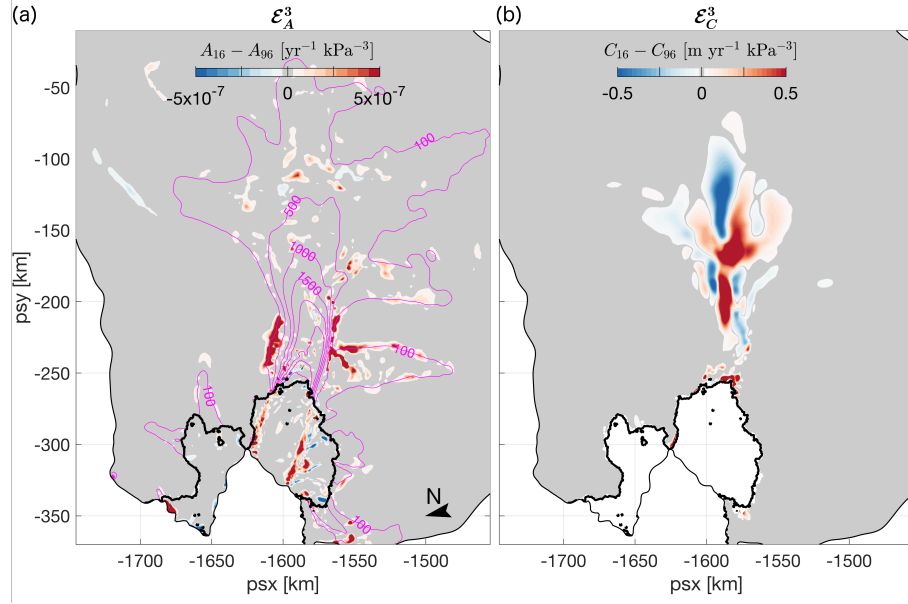


Figure 4. (a) Results for the \mathcal{E}_A^3 experiment: changes in the rate factor A required to fully ~~explain the reproduce~~ observed changes in surface speed of the ice shelf and grounded ice between years 1996 and 2016. The sliding exponent $m = 3$ and basal slipperiness C ~~are were~~ kept fixed ~~between 1996 and 2016. for grounded areas.~~ Magenta contours (in m/yr) correspond to the surface speed in 2016. (b) Results for the \mathcal{E}_C^3 experiment: changes in the basal slipperiness C required to explain the observed increase in surface speed of the grounded ice between 1996 and 2016. The rate factor A is assumed constant between 1996 and 2016.

geographical areas: a localized increase within the shear margins of the ice shelf, and a more widespread increase along the slower-moving flanks (magenta contours in Fig. 4a indicate surface speed in 2016) of the main glacier and westernmost tributary, about 20 km upstream of the 2016 grounding line. Changes within the ice shelf shear margins are consistent with their increasingly complex and damaged morphology, as is apparent from satellite images (Alley et al., 2019). Weakening of the ice in these areas ~~accounts is sufficient to account~~ for the remaining 50% of observed changes in ice-shelf speed-up that could not previously be explained by calving and ice shelf thinning alone (experiment $\mathcal{E}_{\text{CalThin}}^3$). Projected changes in A along the flanks of the upstream glacier, on the other hand, are more ambiguous. Values in excess of $10^{-7} \text{ yr}^{-1} \text{ kPa}^{-3}$ correspond to an equivalent increase in ‘ice’ temperature by up to 40°C . This is nonphysical unless (part of) the change is attributed to damage or evolution of the ice fabric. Based on our analysis of Sentinel and Landsat satellite images, there is no obvious indication of recent changes in the surface morphology in these areas. Either significant and wide-spread changes in the thermal and mechanical properties have occurred beneath the surface, or the observed speed-up and thinning in these areas, as previously reported by Bamber and Dawson (2020), cannot be convincingly attributed to changes in the rate factor.

Alternatively, temporal changes in C can be invoked to explain the discrepancies between modeled and observed changes in surface speed between years 1996 and 2016. Results presented in Fig. 4b suggest that a complex and widespread pattern of changes in the slipperiness is required across an extensive portion of PIG’s central basin and its upper catchment. Despite

the complex and poorly understood relationship between C and quantifiable physical properties of the ice/bed interface, it is difficult to understand how any single process or combination of physical processes could be responsible for the large and widespread changes in C over a time period of two decades. Further information, such as a timeseries of maps similar to Fig. 4b, can potentially be used to test the robustness of this result and provide further insights into the physical processes that could control such changes. This is the subject of future research.

We note that in the \mathcal{E}_C^3 experiment, velocities on the floating ice shelf were largely unaffected by changes in C , and remained significantly slower than observations (not shown). In contrast, changes in the rate factor were able to fully account for the speed-up of the ice shelf. On the other hand, large variations in A were needed to explain the changes in ice dynamics along the slow-moving flanks of PIG (Fig. 4a), whereas only small changes in C less than $10^{-3} \text{ yr}^{-1} \text{ kPa}^{-3} \text{ m}$ were required to explain this behaviour. It is therefore conceivable that, in addition to PIG's evolving geometry, an intricate combination of changes in both the rate factor and basal slipperiness are required to explain the glacier's complex and spatially-diverse patterns of speed-up over the last two decades. It is however not straightforward to disentangle these processes in the current modeling framework.

3.3 Evidence for a heterogeneous bed rheology

The relationship between changes in geometry and the dynamic response of a glacier crucially depends on the mechanical properties of the underlying bed and subglacial hydrology. So far, we have assumed that basal sliding can be represented by a ~~viseous power-law~~ non-linear viscous power-law with spatially uniform stress exponent $m = 3$ (see Eq. 3). A ~~viseous~~ power law rheology is particularly suitable for the description of hard-bedded sliding without cavitation (Weertman, 1957), but missing processes such as variations in effective pressure or the deformation of a subglacial till layer with a maximum shear (yield) stress could be important limitations. Some evidence has been provided for plastic bed properties underneath ice streams either from observations (Tulaczyk et al., 2000; Minchew et al., 2016) or laboratory experiments (Zoet and Iverson, 2020). Most recently, Gillet-Chaulet et al. (2016), Brondex et al. (2019) and Joughin et al. (2019) used numerical simulations to show that different sliding laws can cause a distinctly different dynamical response of PIG to changes in geometry, and observed changes in surface velocity were best reproduced for sliding exponents $m \gg 1$ or using a hybrid law that combines ~~Weertman power-law~~ with Coulomb sliding. Although the results are compatible with a plastic bed underlying the central trunk of PIG, no constraints on the spatial variability in basal rheology were derived.

In order to quantify how different values of the sliding exponent affect the sensitivity of PIG to changes in geometry across the catchment, we repeated perturbation experiments $\mathcal{E}_{\text{CalvThin}}^m$ for a range of sliding law exponents, from $m = 1$ to $m = 21$ at increments of two. Results for $m = 1, 7$ and 13 are shown in Fig. 5. A linear rheology induces a simulated response to calving and thinning that explains less than 50% of the observed changes everywhere. For $m = 7$, relative changes in flow speed exceed 100% along significant portions of the slower-flowing tributaries. For $m = 13$, which effectively corresponds to a plastic rheology, the modeled response overshoots observations by more than 100% in most areas, except along the main glacier, where the response approaches 100%. Across the model domain, a significant positive correlation exists between m and relative velocity changes, indicating a stronger dynamic response to perturbations in geometry with increasing values of

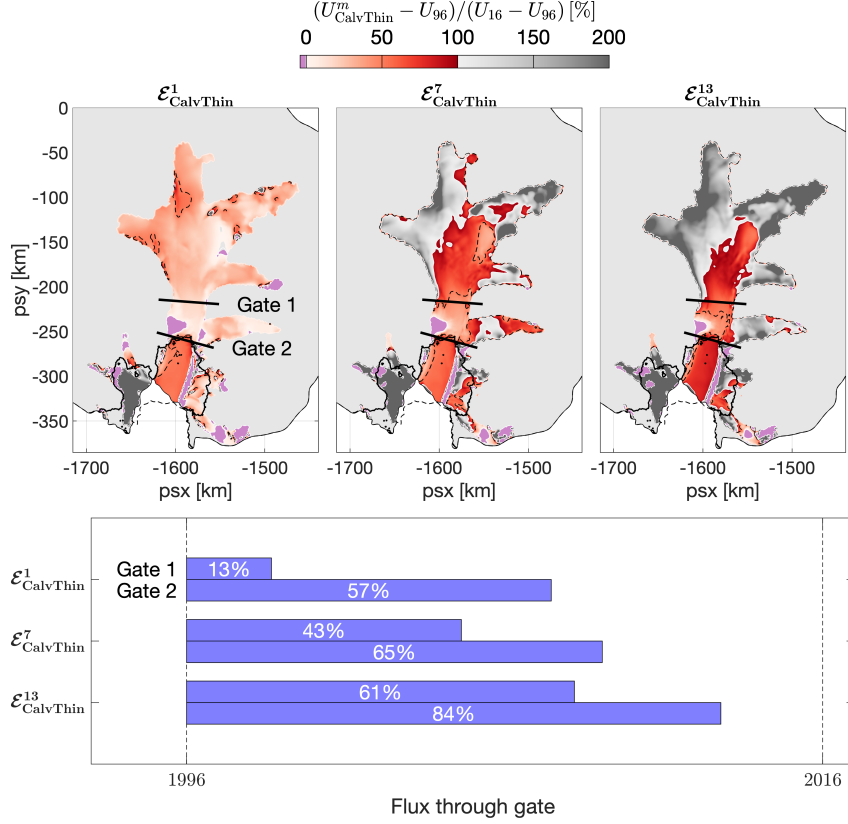


Figure 5. Dependency of simulated-versus-observed changes in surface speed on the sliding law exponent: (a) $m = 1$, (b) $m = 7$ and (c) $m = 13$. Dashed black lines correspond to the 50% contour. Larger values of m cause an increased response of the modeled surface speed to geometrical changes (calving, thinning and grounding line retreat). For $m > 3$, the modeled response of slow-flowing ice in the upstream catchment exceeds observed changes by more than 2-fold, whereas for $m = 13$, modeled changes of the fast-flowing central trunk are still smaller than observed changes. (d) Changes in flux through Gate 1 and 2 as a percentage of observed changes for $m = 1, 7$ and 13 .

m . This finding is in agreement with Gillet-Chaulet et al. (2016) and Joughin et al. (2019), however our maps show that no single, spatially uniform value of the sliding exponent is able to produce a good match between model output and observations across the entire catchment.

The positive correlation between the flow response and m is an inherent property of the adopted physical description of glacier dynamics. For the shallow ice stream approximation with a non-linear **Weertman-viscous** sliding law, the first-order response of the surface velocity, δU , to small perturbations in surface elevation, δS , was previously determined by Gudmundsson (2008) and depends on m in the following non-linear way :

$$\delta U \equiv |\mathcal{T}_{US}(m)|\delta S = \frac{f_1 m}{m + f_2} \delta S. \quad (4)$$

The transfer amplitude $|\mathcal{T}_{US}|$ contains complicated positive functions f_1 and f_2 that generally depend on the wavelength of the surface perturbation, geometrical factors such as the local bed slope, and the basal slipperiness C . Further details are provided in App. C. Despite the simplifying assumptions that underlie the analytical expression of $|\mathcal{T}_{US}|$ obtained by Gudmundsson (2008), results from our simulations $\mathcal{E}_{\text{CalvThin}}^{m_i}$, $m_i \in \{1, 3, \dots, 21\}$, indicate that Eq. 4 is also applicable to the more complex setting of PIG. Indeed, as explained in detail in App. C, we found that across a large portion of the PIG catchment, the transfer amplitude $|\mathcal{T}_{US}|$ provides a suitable model to describe the dependency of the relative velocity changes $\Delta U_{\text{CalvThin}}/\Delta U$ on m . The parameters f_1 and f_2 were treated as spatially variable fields, and best estimates for $f_1(\mathbf{x})$ and $f_2(\mathbf{x})$ were obtained by minimizing the misfit between $\frac{f_1(\mathbf{x})m}{m+f_2(\mathbf{x})}$ and $\frac{\Delta U_{\text{CalvThin}}^{m_i}(\mathbf{x})}{\Delta U}$ with $m_i \in \{1, 3, \dots, 21\}$.

Given the $f_1^*(\mathbf{x})$ and $f_2^*(\mathbf{x})$ were obtained as a solution of the minimization problem

$$(f_1^*(\mathbf{x}), f_2^*(\mathbf{x})) = \min_{f_1, f_2} \left(\frac{f_1(\mathbf{x})m}{m+f_2(\mathbf{x})} - \frac{\Delta U_{\text{CalvThin}}^m(\mathbf{x})}{U_{16} - U_{96}} \right), \text{ with } m \in \{1, 3, \dots, 21\}. \quad (5)$$

The non-linear dependency of $\Delta U_{\text{CalvThin}}/\Delta U$ on m with known fields $f_1(\mathbf{x})$ and $f_2(\mathbf{x})$ can then be approximated by

$$\frac{\Delta U_{\text{CalvThin}}^m}{U_{16} - U_{96}} \approx \frac{f_1^*(\mathbf{x})m}{m+f_2^*(\mathbf{x})}, \quad (6)$$

Using this dependency of the simulated velocity changes on m , one can derive an ‘optimal’-‘optimal’ spatial distribution of the sliding exponent, $m_{\text{optimal}}(\mathbf{x})$, such that $\Delta U_{\text{CalvThin}}/\Delta U = 100\% \cdot \Delta U_{\text{CalvThin}}/(U_{16} - U_{96}) = 100\%$ everywhere, namely

$$m_{\text{optimal}}(\mathbf{x}) = \frac{100f_2(\mathbf{x})}{f_1(\mathbf{x}) - 100} \frac{f_2^*(\mathbf{x})}{f_1^*(\mathbf{x}) - 1}. \quad (7)$$

By construction, the variable sliding exponent $m_{\text{optimal}}(\mathbf{x})$ enables to reproduce 100% of the observed speed-up of PIG in response to calving and ice thickness changes. The results, depicted in Fig. 6a, indicate that plastic bed conditions ($m \gg 1$) prevail across most of the fast-flowing central valley and parts of the upstream tributaries. Values generally increase towards the grounding line, whilst linear or weakly non-linear bed conditions are consistently found in the slow-flowing inter-tributary areas. This finding is compatible with the presence of a weak, water saturated till beneath fast-flowing areas of PIG, and hard bedrock or consolidated till between tributaries (Joughin et al., 2009). The transition to lower exponents in areas with slower flow ($< 600 \text{ m a}^{-1}$) is also consistent with results based on a Coulomb-limited sliding law, which produces Coulomb plastic behaviour at speeds $> 300 \text{ m a}^{-1}$ and weakly non-linear viscous sliding at slower speeds (Joughin et al., 2019).

Two interesting properties of the regression model in Eq. 4 are worth noting. Firstly, for $m \rightarrow \infty$, the function $|\mathcal{T}_{US}|$ approaches a horizontal asymptote with limit equal to f_1 . As a consequence, the associated solution for m_{optimal} diverges to ∞ for locations x where $f_1(x) = 100$ $f_1^*(x) = 100$, and becomes negative where $f_1(x) < 100$ $f_1^*(x) < 100$. In these areas, indicated by black dots in Fig. 6a, no non-negative, finite value of m exists such that $\Delta U_{\text{CalvThin}}(x)/\Delta U(x) = 100\% \Delta U_{\text{CalvThin}}(x)/(U_{16} - U_{96}) =$ and conventional Weertman sliding is unable to fully reproduce the observed flow changes in response to thickness changes and calving. Either a different form of the sliding law is required, or additional changes in the rate factor A and/or basal

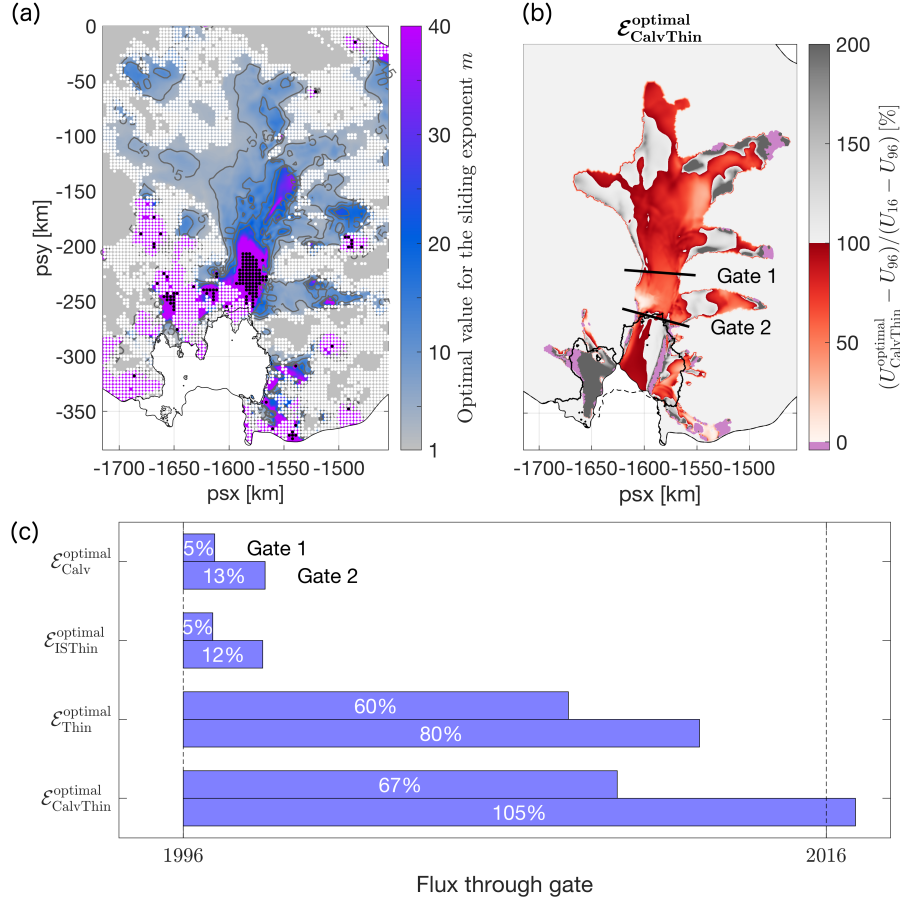


Figure 6. (a) Optimal values of the sliding exponent, required to ensure close agreement between modeled and observed changes in flow velocity of Pine Island Glacier between years 1996 and 2016. White and black dots mark areas where such an agreement cannot be achieved for different reasons: white dots indicate a poor fit between the transfer function $|\mathcal{T}_{US}|$ and $\Delta U_{\text{CalvThin}}^{m_i} / \Delta U, m_i \in \{1, 3, \dots, 21\} \Delta U_{\text{CalvThin}}^{m_i} / (U_{16} - U_{96}), m_i \in \{1, 3, \dots, 21\}$, with $R^2 < 0.9$; black dots indicate areas where a positive, finite solution for m_{optimal} in Eq. 7 does not exist, and Weertman non-linear viscous sliding cannot reproduce observed changes in surface flow. (b) Same as Fig. 3d but for optimal values of the sliding law exponent in panel a. (c) Same as Fig. 3e but for optimal values of the sliding law exponent in panel a.

slipperiness C are needed. These findings are the subject of a forthcoming study. Our second observation concerns locations where ΔU either contains U_{16} or U_{96} contain significant measurement uncertainties, or approaches the limit $\Delta U \rightarrow 0$, where no discernible changes in the surface velocity were measured, i.e. $U_{16} - U_{96} \approx 0$. In these areas, the non-linear regression was generally found to be poor, with R^2 values smaller than 0.9 as indicated by the white dots in Fig. 6a. As no reliable estimate for m_{optimal} could be obtained for areas shaded in white or black in Fig. 6a, values were instead based on a nearest-neighbour interpolation.

445 It is important to reiterate that the used regression method crucially relies on non-trivial measurements of changes in surface velocity ($\Delta U \neq U_{16} - U_{96} \neq 0$), and cannot be used to retrieve information about the basal rheology of ice bodies that are presently in steady state. It should also be noted that values of $f_1(\mathbf{x})$ and $f_2(\mathbf{x})$ were derived independently for each node of the computational mesh, whereas the continuum mechanical properties of glacier flow would suggest a non-zero spatial covariance $\langle f_1(x_1), f_1(x_2) \rangle \neq 0$ and $\langle f_2(x_1), f_2(x_2) \rangle \neq 0$. The optimal solution for m is therefore not automatically
 450 mesh independent or robust with respect to the amount of regularization in the inversion. This concern is discussed further in App. D.

In order to demonstrate the improved model response to thinning and calving for a spatially variable sliding exponent $m_{\text{optimal}}(\mathbf{x})$, we performed a new inversion with $m_{\text{optimal}}(\mathbf{x})$, and subsequently repeated the geometric perturbation experiments $\mathcal{E}_*^{\text{optimal}}$. The results are presented in Fig. 6b and c. Compared to spatially uniform values of m (Fig. 3d and Fig. 5),
 455 a spatially variable basal rheology generally improves the fit between observed changes in flow and the modeled response across the entire basin. Based on the flux changes through Gate 1 and 2, we find that (1) calving and ice thickness changes in combination with a spatially variable, predominantly plastic bed rheology account for 67% and 105% of flux changes through Gate 1 and 2 respectively, compared to 28% and 64% for a uniform non-linear viscous sliding law with exponent $m = 3$, that (2) calving and ice shelf thinning caused an almost identical response in ice dynamics upstream of the grounding line,
 460 and that (3) dynamic thinning and grounding line movement account for most of the flux changes between years 1996 and 2016. The remaining mismatch between the observed and modeled response in Fig. 6b can, at least in part, be attributed to uncertainties in $m_{\text{optimal}}(\mathbf{x})$. This is of particular relevance in the vicinity of the grounding line and for parts of the central trunk, where the non-linear regression method in Eq. 4 did not provide a reliable or finite estimate for m_{optimal} , ~~and where Weertman theory of sliding could break down all together (Iverson et al., 1998; Schoof, 2006).~~ Previous studies, e.g. by Gillet-Chaulet et al. (2016) and Joughin et al. (2019) have demonstrated a better agreement between modeled and observed speed-up using Coulomb-limited sliding laws, such as those proposed by Budd et al. (1984); Schoof (2006); Tsai et al. (2015). Our results are consistent with these earlier studies, and suggest that power-law sliding does not adequately capture the physical relationship between basal shear stress and sliding in the vicinity of the grounding line.

4 Conclusions

470 Based on the most comprehensive observations of ice shelf and grounded ice thickness changes to date, and a suite of diagnostic model experiments with the contemporary flow model Úa, we have analyzed the relative importance of ice shelf thinning, calving and grounding line retreat for the speed-up of Pine Island Glacier ~~between years over the period~~ 1996 ~~and to~~ 2016. The detailed comparison between simulated and observed changes in flow speed has provided ~~unprecedented~~ insights into the ability of a modern-day ice flow model to reproduce dynamic changes in response to prescribed geometric perturbations.
 475 Significant discrepancies between observed and modeled changes in flow were found, and were addressed by either allowing changes in ice viscosity and basal slipperiness, or by varying the mechanical properties of the ice-bed interface. For non-linear viscous sliding at the bed, geometric perturbations could only account for 64% of the observed flux increases close to the

grounding line, whereas the remaining 36% could be attributed to large and widespread changes in ice viscosity (including damage) and/or changes in basal slipperiness. Under the alternative assumption that ice viscosity and basal slipperiness did not change considerably over the last two decades, we found that the recent increase in flow speed of Pine Island Glacier is only compatible with observed patterns of thinning if a heterogeneous, predominantly plastic bed underlies large parts of the central glacier and its upstream tributaries, [consistent with earlier literature](#).

Code and data availability. The open-source ice flow model Úa is available from Gudmundsson (2020). All model configurations files specific to this study, as well as model output and plotting routines for each figure are available from DOI TBC. Ice shelf thinning rates are available upon request from FP.

Appendix A: Observations of Pine Island Ice Shelf thickness changes between 1996 and 2016

We derived a new ice-shelf height time series from measurements acquired by four overlapping ESA satellite radar altimetry (RA) missions: ERS-1 (1991–1996), ERS-2 (1995–2003), Envisat (2002–2012), and CryoSat-2 (2010–present). For this study, we constructed a record of ice-shelf height spanning 20 years (1996–2016), with a temporal sampling of 3 months. We integrated all measurements along the satellite ground tracks and gridded the solution on a 3 by 3 km grid.

Our adopted processing steps for RA data are a modification/improvement from Paolo et al. (2016) and Nilsson et al. (2016). Specifically for CryoSat-2, we retracked ESA’s SARIn L1B product over the Antarctic ice shelves using the approach by Nilsson et al. (2016); we corrected for a 60 m range offset for data with surface types ‘land’ or ‘closed sea’; and removed points with anomalous backscatter values (>30 dB). We estimated heights with a modified (from McMillan et al. (2014)) surface-fit approach, with a variable rather than constant search radius to account for the RA heterogeneous spatial distribution, and calculating mean values along the satellite reference tracks; we removed height estimates less than 2 m above the Eigen-6C4 geoid (Chuter and Bamber, 2015) to account for ice-shelf mask imperfections near the calving front; applied all of the standard corrections to altimeter data over ice shelves (for example, removed gross outliers, and residual heights with respect to mean topography > 15 m; ran an iterative three-sigma filter; minimized the effect of variations in backscatter (Paolo et al., 2016); corrected for ocean tides (Padman et al., 2002) and inverse barometer effects (Padman et al., 2004).

We then gridded the height data in space and time on a $3\text{ km} \times 3\text{ km} \times 3\text{ month}$ cube, for each mission independently. We merged the records (all four satellites) by only accepting time series that overlapped by at least three quarters of a year to ensure proper cross-calibration, and removed (and subsequently interpolated) anomalous data points that deviated from the trend by more than 5 std. This removes data with, for example, satellite mispointing, anomalous backscatter fluctuations, grounded-ice contamination, high surface slopes and geolocation errors. We fitted linear trends to the gridded product to obtain the ΔH field used in our model experiments (see Sect. 2.1). We also removed a 3 km buffer around the ice-shelf boundaries to further mitigate floating-grounded mask imperfections, and the limitation of geophysical corrections within the ice-shelf flexural zone.

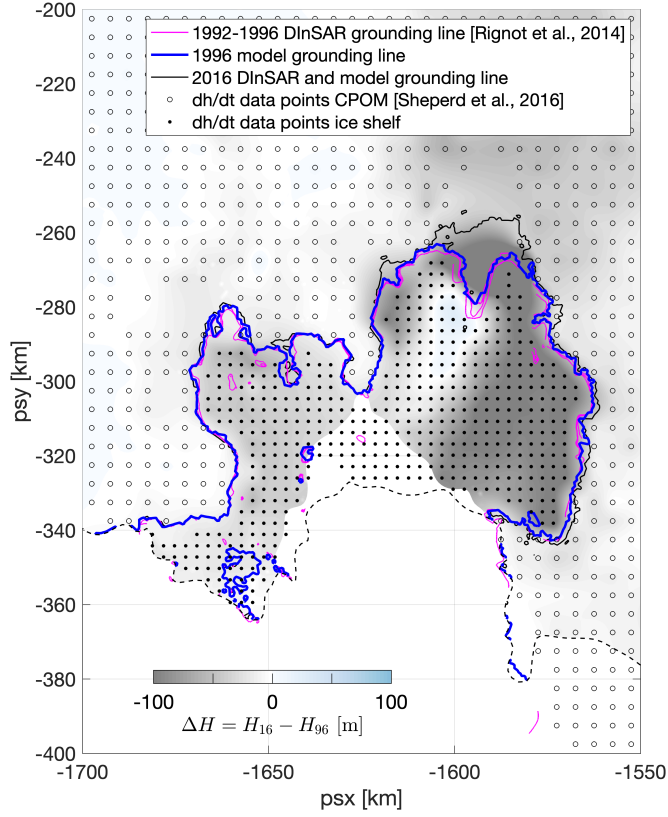


Figure A1. Ice thickness changes (ΔH) between 1996 and 2016, based on a comprehensive analysis of satellite altimeter data. The altimeter data coverage is represented by dots (ice shelf) and circles (grounded ice, (Shepherd et al., 2016)). The final 1996 ice thickness distribution was obtained by subtracting ΔH from the 2016 Bedmachine ice thickness (Morlighem et al., 2020), as described in Sect.2.1. The associated 1996 grounding line location (blue line) compares well to independent DInSAR measurements (magenta line, (Rignot et al., 2014)).

Appendix B: ~~Model configuration and inverse methodology~~

510 The thickness changes for the ice shelf were combined with existing data for thickness changes over the same time period on the grounded ice (Shepherd et al., 2016). The resulting dataset for ΔH , as used in the experiments described in Sect. 2.2, is shown in Fig. A1. The figure shows the data grids, including the 3 km buffer downstream of the 1996 grounding line, and other data sparse areas along the central flowline. Here, thickness changes were obtained through linear interpolation from neighbouring data. The grounding line location associated with our 1996 thickness distribution was compared to independent measurements from DInSAR (Rignot et al., 2014), and both agree well (Fig. A1).

515 Appendix B: Model configuration and optimization

The open source ice flow model Úa (Gudmundsson, 2020) uses finite element ~~methods~~ method to solve the shallow ice stream equations, commonly referred to as SSA or SSTREAM (Hutter, 1983; MacAyeal, 1989), on an irregular triangular mesh. The diagnostic velocity solver is based on an iterative Newton-Raphson method. A fixed mesh with 109,300 linear elements was used with a median nodal spacing of 1.2 km and local mesh refinement down to 500 m in areas with above-average horizontal shear, strong gradients in ice thickness and within a 10 km buffer around the grounding line. The mesh was generated using the

open-source generator mesh2d (Engwirda, 2014). The ~~inverse optimization~~ capabilities of Úa follow commonly applied techniques in ice flow modeling to optimize uncertain model parameters, p_i , based on prior information, \hat{p}_i , and a range of observations with associated measurement errors (MacAyeal, 1992). Úa uses an adjoint method to obtain a combined optimal estimate of the spatially varying rate factor A and basal slipperiness C across the full model domain, for given observations of surface velocity u_{obs} and measurement errors ε_u . Optimal values for $p_i \in \{A, C\}$ were obtained as a solution to the minimization problem $d_p J$ with the cost function J defined as the sum of the misfit term I and Tikhonov regularization R : $J = I + R$, with

$$I = \frac{1}{2\mathcal{A}} \int d\mathbf{x} (u_{\text{model}} - u_{\text{obs}})^2 / \varepsilon_u^2, \quad (\text{B1})$$

$$R = \frac{1}{2\mathcal{A}} \int d\mathbf{x} \sum_i \left(\gamma_{i,s}^2 (\nabla \log_{10}(p_i / \hat{p}_i))^2 + \gamma_{i,a}^2 (\log_{10}(p_i / \hat{p}_i))^2 \right), \quad (\text{B2})$$

and $\mathcal{A} = \int d\mathbf{x}$ the total area of the model domain. ~~A priori values of the rate factor and slipperiness were chosen as $\hat{A} = 5.04 \times 10^{-9} \text{ kPa}^{-3} \text{ yr}^{-1}$ which corresponds to a spatially uniform ice temperature of -15°C (Cuffey and Paterson, 2010), and $\hat{C} = u_b \tau^{-m}$, with $u_b = 750 \text{ m yr}^{-1}$ and $\tau = 80 \text{ kPa}$ and m the sliding law exponent. An iterative interior point optimization algorithm was used to calculate $d_p J$ and stopped after 10^4 iterations, when fractional changes to the cost function were less than 10^{-5} . An optimal value for the Tikhonov regularization multiplier, γ_s , in the cost function was~~

~~The gradient and amplitude contributions in the regularization term (Eq. B2) are multiplied by spatially-constant Tikhonov regularization multipliers, $\gamma_{i,s}$ and $\gamma_{i,a}$. Optimal values for $\gamma_{i,s}$ and $\gamma_{i,a}$ were determined using an L-curve approach, as. For $\gamma_{i,s}$ results are shown in Fig. B1. The value values $\gamma_s = 25000$ $\gamma_{A,s} = \gamma_{C,s} = 25000 \text{ m}$ was were used for all experiments in the main part of the text, as it produced the smallest misfit between observed and modelled surface velocities whilst limiting the risk of overfitting. The sensitivity of the main results with respect to the choice of γ_s is discussed in App. D. A similar L-curve approach was followed to determine an optimal values for $\gamma_{i,a}$, with $\gamma_{A,a} = \gamma_{C,a} = 1$ used throughout this study.~~

~~The pre-multipliers $\gamma_{i,s}$ and $\gamma_{i,a}$ are constant across the model domain. Some studies set $\gamma_{A,a} = \gamma_{A,s} = 0$ for grounded areas, and only optimize the rate factor on the ice shelves. This approach assumes perfect prior knowledge about the spatial distribution and magnitude of the rate factor upstream of the grounding line, often tied to (uncertain) estimates of ice temperature. Here we prefer to optimize A across the full domain to allow for spatial variations in ice temperature, damage, fabric and other ice properties for both floating and grounded ice. The amplitude and gradient of A , relative to a spatially constant prior value, are controlled by $\gamma_{A,a}$ and $\gamma_{A,s}$ respectively, with optimal values given above.~~

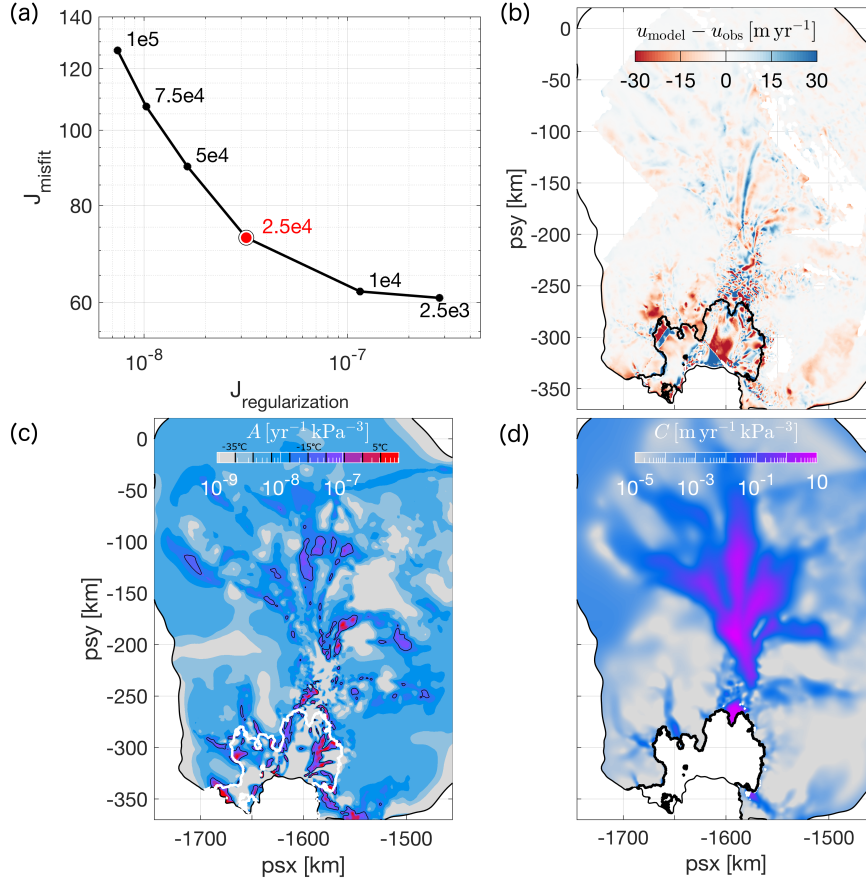


Figure B1. (a) L-curve used to determine the optimal value of the Tikhonov regularization multiplier γ_s , highlighted in red. (b) Misfit between modeled and observed surface speed in 1996 for $\gamma_s = 25000$ m. (c) Rate factor (A in Eq. 2) in 1996, obtained as a minimum of the cost function J in Eq. B1 with $\gamma_s = 25000$ m. The equivalent depth-averaged ice temperature ranges from -35 °C (grey) to 5 °C (red). Colors are discretized at 5 °C intervals and the black lines indicate the 0 °C contour. The white line corresponds to the 1996 grounding line position. (d) Optimal value of the basal slipperiness (C in Eq. 3) in 1996, estimated using the adjoint minimization approach.

All results presented here are based on optimization experiments with spatially constant a priori values for the rate factor and slipperiness: $\hat{A} = 5.04 \times 10^{-9} \text{ kPa}^{-3} \text{ yr}^{-1}$, which corresponds to a spatially uniform ice temperature of -15 °C (Cuffey and Paterson, 2010), and $\hat{C} = u_b \tau^{-m}$, with $u_b = 750 \text{ m yr}^{-1}$ and $\tau = 80 \text{ kPa}$ and m the sliding law exponent. Different a priori values for the rate factor, equivalent to ice temperatures between -20 °C and -5 °C, were tested, but did not cause significant differences in the results. We did not consider optimization experiments with spatially variable \hat{A} based on independent estimates of ice temperature and/or damage, since such estimates contain significant uncertainties at the regional scales considered in this study.

Figure B1 shows the difference between u_{model} and u_{obs} (panel b). Figures B1b-d summarize the results for an optimization with $\gamma_{is} = 25000 \text{ m}$, $\gamma_{ia} = 1$, $\hat{A} = 5.04 \times 10^{-9} \text{ kPa}^{-3} \text{ yr}^{-1}$ and corresponding optimal estimates of A (panel c) and C (panel d) for $\gamma_s = 25000 \text{ m}$, $\hat{C} = 1.46 \times 10^{-3} \text{ m yr}^{-1} \text{ kPa}^{-3}$. Modeled surface velocities are typically within 30 meters per year or less of the observed values, with a mean misfit of -1.68 m yr^{-1} and standard deviation of 15.3 m yr^{-1} . The highest values of the rate factor are generally found within the shear margins, with positive equivalent ice temperatures suggesting the presence of a complex rheology or damage. The highest values of the slipperiness are consistently found in the fast-flowing central part of the glacier and along its upstream tributaries, with noticeably reduced values of C in an area between 5 and 40 km upstream of the 1996 grounding line. These results are broadly in agreement with previously published maps, see e.g. Arthern et al. (2015).

Appendix C: Non-linear dependency of the flow response on the sliding exponent

The transfer amplitude $|\mathcal{T}_{US}|$, defined in Eq. 4, describes the linear response of the along-slope surface velocity to small harmonic perturbations in the surface elevation or, equivalently, ice thickness. Analytical solutions for the transfer function \mathcal{T}_{US} (amplitude and phase) in the framework of the shallow ice stream approximation with a linear ice rheology ($n = 1$ in Eq. 2) and a non-linear viscous Weertman sliding law (arbitrary m in Eq. 3) were previously obtained by Gudmundsson (2008). Note that the original expression (Eq. 29 in Gudmundsson (2008)) contained a printing error so we repeat the correct form here:

$$\mathcal{T}_{US} = \frac{\tau_d [m\gamma(1+\psi) + \eta H (j^2\psi + k^2 + 4l^2)]}{Hm\gamma^2 + \gamma\eta H^2 [l^2(4+m) + k^2(1+4m)] + 4H^3 j^4 \eta^2}, \quad (\text{C1})$$

where H is the local ice thickness, α is the local bed slope, ρ is the ice viscosity, $\tau_d = \rho g H \sin \alpha$ is the driving stress, η is the effective viscosity and $\gamma = \frac{\tau_d^{1-m}}{mC}$, $\psi = ikH \cot \alpha$ and $j^2 = k^2 + l^2$ are abbreviations, with k and l the along-slope and transverse wavelength respectively of the harmonic surface perturbation. Since we focus on the instantaneous response of the velocity to perturbations at the surface, the exponential decay of \mathcal{T}_{US} with time has been omitted. An equivalent expression for the response of the transverse velocity component can be derived; we refer to Gudmundsson (2008) for more details.

Following Gudmundsson (2008), physical quantities can be rescaled to obtain the non-dimensional form of the transfer function. After substitution of the scalings $H \rightarrow 1$, $\eta \rightarrow 1/2$, $\tau_d \rightarrow 1$ into Eq. C1 and some reordering, one obtains

$$\mathcal{T}_{US} = \frac{m \left[\frac{1}{C} (1+\psi) + \frac{1}{2} (j^2\psi + k^2 + 4l^2) \right]}{m \left[j^4 + \frac{1}{2C} (l^2 + 4k^2) \right] + \frac{1}{C^2} + \frac{1}{2C} (4l^2 + k^2)}. \quad (\text{C2})$$

The resulting transfer amplitude takes the form $|\mathcal{T}_{US}| = \frac{f_1 m}{m+f_2}$ as in Eq. 4, where functions f_1 and f_2 depend on C , α , k and l .

The analytical expression in Eq. C2 describes the first-order response to small perturbations in ice thickness, $\delta H \ll 1$, for well-defined length scales characterized by k and l . However, in a realistic setting such as PIG, the system responds to a complicated perturbation composed of a range of wavelengths and amplitudes, and Eq. C2 does not automatically hold. Based on experiments $\mathcal{E}_{\text{CalvThin}}^{m_i}$, $m_i \in \{1, 3, \dots, 21\}$ presented in Sect. 3.3, we found that the simulated surface response of PIG to observed geometrical perturbations retains its dependency on m of the form $\frac{f_1 m}{m+f_2}$, but more complicated expressions for f_1 and f_2 are required that do not exist in analytical form. A best-estimate for the spatially varying fields f_1 and f_2 was obtained

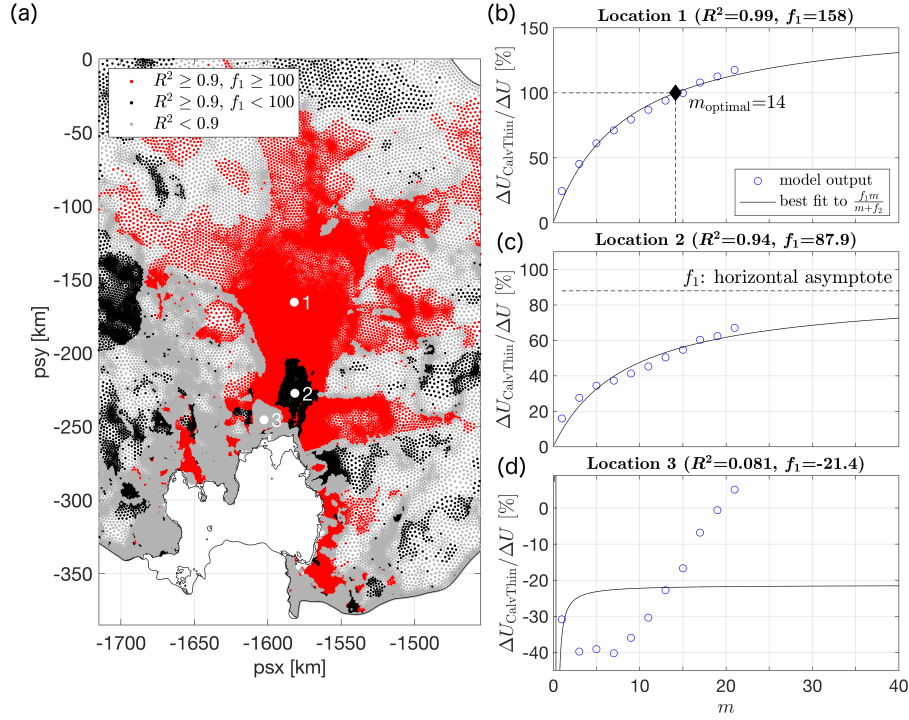


Figure C1. (a) Goodness of fit between $\frac{f_1 m}{m+f_2}$ and model simulations $\frac{\Delta U_{\text{CalvThin}}^{m_i}}{\Delta U}, m_i \in \{1, 3, \dots, 21\}$. Red areas correspond to $R^2 \geq 0.9$ and fitting parameter $f_1 \geq 100$. An example of the fit at location 1 and resulting m_{optimal} (Eq. 7) are shown in panel b. Black areas in (a) correspond to $R^2 \geq 0.9$ and fitting parameter $f_1 < 100$. The horizontal asymptote with limit < 100 indicates that a positive, finite solution m_{optimal} does not exist, and Weertman sliding cannot reproduce 100% of the observed changes in surface velocity. An example of the fit and asymptote at location 2 are shown in panel c. Grey areas in (a) correspond to $R^2 < 0.9$, indicating a poor fit between $\frac{f_1 m}{m+f_2}$ and $\frac{\Delta U_{\text{CalvThin}}^{m_i}}{\Delta U}, m_i \in \{1, 3, \dots, 21\}$. An example at location 3 is shown in panel d.

585 by minimizing the misfit between $\frac{\Delta U_{\text{CalvThin}}^{m_i}}{\Delta U}, m_i \in \{1, 3, \dots, 21\}$ and $\frac{\Delta U_{\text{CalvThin}}^{m_i}}{(U_{16} - U_{96})}, m_i \in \{1, 3, \dots, 21\}$ and $\frac{f_1 m}{m+f_2}$. The resulting misfit, quantified by R^2 values, is summarized in Fig. C1a. Red and black areas indicate a good fit with $R^2 \geq 0.9$, though an important distinction was made between solutions with $f_1 \geq 100$ (red) and $f_1 < 100$ (black). The difference between both cases is explained further in Sect. 3.3. Examples of the fit at locations 1 and 2 are shown in Fig. C1b and c respectively. Grey shading in Fig. C1a corresponds to a poor fit ($R^2 < 0.9$) and the dependency of $\frac{\Delta U_{\text{CalvThin}}^m}{(U_{16} - U_{96})}$ on m cannot be adequately described by the function $\frac{f_1 m}{m+f_2}$. Possible reasons for this discrepancy are discussed in Sect. 3.3.

590

Appendix D: Dependency of the results on the regularization

The inverse problem of inferring information about the rate factor A and basal slipperiness C from uncertain observations of surface velocity is generally ill-posed. To remedy the ill-posedness of the problem, additional information in the form of a regularization term (Eq. B2) is commonly added to the cost function. ~~In a Bayesian framework, the regularization plays the role of a prior and is added to the misfit, which corresponds to the likelihood.~~ The solution of the minimization problem generally depends on the choice of regularization. In the specific case of a Tikhonov regularization, which is used throughout this study, the solution for A and C will depend on the unknown ~~multiplier γ_s~~ multipliers $\gamma_{i,a}$ and $\gamma_{i,s}$, and the choice of prior information \hat{p}_s in Eq. B2. One method to choose an ‘optimal’ value for ~~γ_s~~ the multipliers is the L-curve approach presented in App. B. However, this is an ad-hoc method and it remains to be shown that results are robust for a range of ~~γ_s values.~~ γ values. Below we discuss the robustness of our results for a range γ_s values. A similar analysis was carried out for a range of γ_a values and priors, but those results did not affect our conclusions and are not shown here.

In case of the perturbation experiments \mathcal{E}_*^3 , which were designed to simulate the velocity response to a series of prescribed changes in the PIG geometry, we are primarily interested in the γ_s -dependency of the relative fluxes in Fig. 3e. In addition to the experiments with default value $\gamma_s = 25000\text{m}$, identical perturbation experiments were carried out for $\gamma_s = 10000\text{m}$ and $\gamma_s = 50000\text{m}$. The corresponding changes in flux, presented in Table D1, do not show any significant variability with γ_s and results presented in Sect. 3.1 can be considered robust, at least across the range of tested γ_s values.

Experiments \mathcal{E}_A^3 and \mathcal{E}_C^3 were also repeated for $\gamma_s = 10000\text{m}$ and $\gamma_s = 50000\text{m}$. Maps of A and C (not shown) were compared to the default results for $\gamma_s = 25000\text{m}$ shown in Fig. 4, and no significant qualitative differences were found. Perturbation experiments \mathcal{E}_*^m for a range of sliding law exponents $1 \leq m \leq 21$ were repeated for $\gamma_s = 10000\text{m}$ and $\gamma_s = 50000\text{m}$. Following the approach outlined in Sect. 3.3, an optimal spatial distribution of the sliding exponent was computed for each γ_s . Results are presented in Fig. D1 and show a decreasing trend in m_{optimal} for increasing values of the regularization multiplier γ_s . In particular, the area where no positive, finite solution exist for m_{optimal} (shaded in black) is reduced in size and eventually disappears for increasing amounts of regularization. However, the spatial distribution of m_{optimal} is found to be in broad agreement across the considered range of γ_s .

Author contributions. JDR and RR designed and initiated the project and prepared the manuscript; FP processed the ice shelf thickness data; JDR performed the model simulations, carried out the analysis and produced the figures; FP and GHG reviewed and edited the paper.

Competing interests. JDR serves as topical editor for The Cryosphere.

Acknowledgements. We would like to express our sincere appreciation for the thorough reviews by Stephen Cornford, two anonymous reviewers and the editor, Andreas Vieli. Their insightful comments have greatly contributed to a better presentation of our work. JDR,

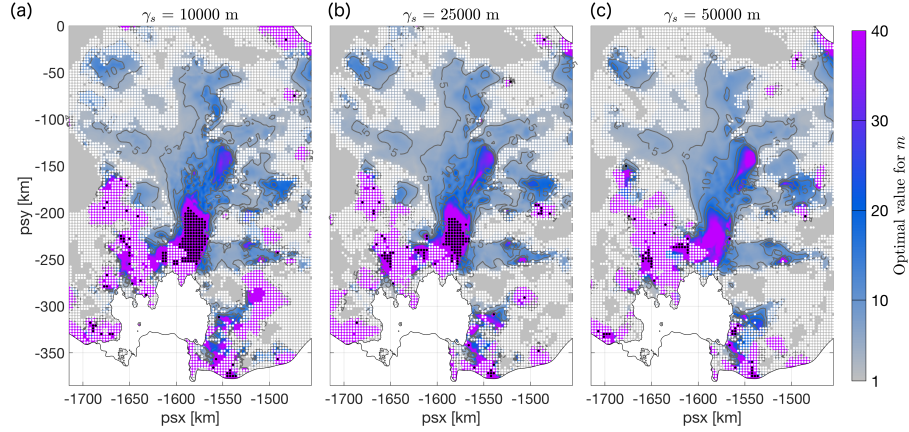


Figure D1. Optimal distribution of m , as in Fig. 6a, for different values of the regularization multiplier: **(a)** $\gamma_s = 10000$ m, **(b)** $\gamma_s = 25000$ m and **(c)** $\gamma_s = 50000$ m. White dots indicate areas where results for the non-linear regression method were poor, with a R^2 -value smaller than 0.9. Black dots indicate areas where the value of f_1 in the fit is less than 100, indicating that agreement between simulated and observed changes in surface velocity cannot be achieved for finite values of m . The value $\gamma_s = 25000$ m was used throughout the main part of this study.

Table D1. Sensitivity of the relative flux changes in the \mathcal{E}_*^3 experiments (see Fig. 3) with respect to the choice of regularization multiplier γ_s . The optimal value, $\gamma_s = 25000$ m, used throughout this study was based on the L-curve presented in Fig. B1.

| | | $\gamma_s = 10000$ m | $\gamma_s = 25000$ m | $\gamma_s = 50000$ m |
|-----------------------------------|--------|----------------------|----------------------|----------------------|
| $\mathcal{E}_{\text{Calv}}^3$ | Gate 1 | 2% | 2% | 2% |
| | Gate 2 | 15% | 13% | 13% |
| $\mathcal{E}_{\text{ISThin}}^3$ | Gate 1 | 2% | 2% | 2% |
| | Gate 2 | 14% | 13% | 12% |
| $\mathcal{E}_{\text{Thin}}^3$ | Gate 1 | 24% | 26% | 25% |
| | Gate 2 | 38% | 45% | 42% |
| $\mathcal{E}_{\text{CalvThin}}^3$ | Gate 1 | 26% | 28% | 27% |
| | Gate 2 | 58% | 64% | 58% |

GHG and RR are supported by the TiPACCs project that receives funding from the European Union's Horizon 2020 research and innovation programme under grant agreement no. 820575. RR is further supported by the Deutsche Forschungsgemeinschaft (DFG) by grant WI4556/3-1 and GHG by the NSFPLR-NERC grant: *Processes, drivers, predictions: Modelling the response of Thwaites Glacier over the next century using ice/ocean coupled models* (NE/S006745/1).

625 References

- Alley, K. E., Scambos, T. A., Alley, R. B., and Holschuh, N.: Troughs developed in ice-stream shear margins precondition ice shelves for ocean-driven breakup, *Science Advances*, 5, 1–8, <https://doi.org/10.1126/sciadv.aax2215>, 2019.
- Arndt, J. E., Larter, R. D., Friedl, P., Gohl, K., Höppner, K., et al.: Bathymetric controls on calving processes at Pine Island Glacier, *The Cryosphere*, 12, 2039–2050, 2018.
- 630 Arthern, R. J. and Williams, C. R.: The sensitivity of West Antarctica to the submarine melting feedback, *Geophysical Research Letters*, 44, 2352–2359, <https://doi.org/10.1002/2017GL072514>, 2017.
- Arthern, R. J., Hindmarsh, R. C., and Williams, C. R.: Flow speed within the Antarctic ice sheet and its controls inferred from satellite observations, *Journal of Geophysical Research F: Earth Surface*, 120, 1171–1188, <https://doi.org/10.1002/2014JF003239>, 2015.
- Bamber, J. L. and Bindshadler, R. A.: An improved elevation dataset for climate and ice-sheet modelling: validation with satellite imagery, *Annals of Glaciology*, 25, 439–444, <https://doi.org/10.3189/S0260305500014427>, 1997.
- 635 Bamber, J. L. and Dawson, G. J.: Complex evolving patterns of mass loss from Antarctica’s largest glacier, *Nature Geoscience*, pp. 1–5, 2020.
- Brondex, J., Gillet-Chaulet, F., and Gagliardini, O.: Sensitivity of centennial mass loss projections of the Amundsen basin to the friction law, *The Cryosphere*, 13, 177–195, 2019.
- 640 Budd, W. F., Jenssen, D., and Smith, I. N.: A Three-Dimensional Time-Dependent Model of the West Antarctic Ice Sheet, *Annals of Glaciology*, 5, 29–36, <https://doi.org/10.3189/1984AoG5-1-29-36>, 1984.
- Christianson, K., Bushuk, M., Dutrieux, P., Parizek, B. R., Joughin, I. R., Alley, R. B., Shean, D. E., Abrahamsen, E. P., Anandakrishnan, S., Heywood, K. J., Kim, T.-W., Lee, S. H., Nicholls, K., Stanton, T., Truffer, M., Webber, B. G. M., Jenkins, A., Jacobs, S., Bindshadler, R., and Holland, D. M.: Sensitivity of Pine Island Glacier to observed ocean forcing, *Geophysical Research Letters*, 43, 10,817–10,825, <https://doi.org/10.1002/2016GL070500>, 2016.
- 645 Chuter, S. J. and Bamber, J. L.: Antarctic ice shelf thickness from CryoSat-2 radar altimetry, *Geophysical Research Letters*, 42, 10 721–10 729, <https://doi.org/10.1002/2015GL066515>, 2015.
- Cuffey, K. and Paterson, W.: *The physics of glaciers*, 4th Edition, [https://doi.org/10.1016/0016-7185\(71\)90086-8](https://doi.org/10.1016/0016-7185(71)90086-8), 2010.
- Dutrieux, P., De Rydt, J., Jenkins, A., Holland, P. R., Ha, H. K., Lee, S. H., Steig, E. J., Ding, Q., Abrahamsen, E. P., and Schröder, M.: Strong sensitivity of Pine Island ice-shelf melting to climatic variability, *Science*, 343, 174–178, 2014.
- 650 Engwirda, D.: Locally-optimal Delaunay-refinement and optimisation-based mesh generation, Ph.D. thesis, The University of Sydney, <http://hdl.handle.net/2123/13148>, 2014.
- Favier, L., Durand, G., Cornford, S., Gudmundsson, G., Gagliardini, O., Gillet-Chaulet, F., Zwinger, T., Payne, A., and Brocq, A.: Retreat of Pine Island Glacier controlled by marine ice-sheet instability, *Nature Clim. Change*, advance online publication, <https://doi.org/10.1038/nclimate2094>, 2014.
- 655 Gardner, A. S., Moholdt, G., Scambos, T., Fahnestock, M., Ligtenberg, S., Van Den Broeke, M., and Nilsson, J.: Increased West Antarctic and unchanged East Antarctic ice discharge over the last 7 years, *Cryosphere*, 12, 521–547, <https://doi.org/10.5194/tc-12-521-2018>, 2018.
- Gillet-Chaulet, F., Durand, G., Gagliardini, O., Mosbeux, C., Mouginot, J., Rémy, F., and Ritz, C.: Assimilation of surface velocities acquired between 1996 and 2010 to constrain the form of the basal friction law under Pine Island Glacier, *Geophysical Research Letters*, 43, 10–311, 2016.
- 660

- Gudmundsson, G. H.: Analytical solutions for the surface response to small amplitude perturbations in boundary data in the shallow-ice-stream approximation, *The Cryosphere*, 2, 77–93, <https://doi.org/10.5194/tc-2-77-2008>, 2008.
- Gudmundsson, G. H.: GHilmarG/UaSource: Ua2019b (Version v2019b), <http://doi.org/10.5281/zenodo.3706623>, 2020.
- Gudmundsson, G. H., Krug, J., Durand, G., Favier, L., and Gagliardini, O.: The stability of grounding lines on retrograde slopes, *Cryosphere*, 6, 1497–1505, <https://doi.org/10.5194/tc-6-1497-2012>, 2012.
- Gudmundsson, G. H., Paolo, F. S., Adusumilli, S., and Fricker, H. A.: Instantaneous Antarctic ice sheet mass loss driven by thinning ice shelves, *Geophysical Research Letters*, 46, 13 903–13 909, <https://doi.org/10.1029/2019GL085027>, 2019.
- Howat, I. M., Porter, C., Smith, B. E., Noh, M.-J., and Morin, P.: The Reference Elevation Model of Antarctica, *The Cryosphere*, 13, 665–674, <https://doi.org/10.5194/tc-13-665-2019>, <https://www.the-cryosphere.net/13/665/2019/>, 2019.
- Hutter, K.: *Theoretical Glaciology: Material Science of Ice and the Mechanics of Glaciers and Ice Sheets*, Mathematical Approaches to Geophysics, Springer, 1983.
- Iverson, N., Hooyer, T., and Baker, R.: Ring-shear studies of till deformation: Coulomb-plastic behavior and distributed strain in glacier beds, *Journal of Glaciology*, 44, 634–642, <https://doi.org/10.3189/s0022143000002136>, 1998.
- Jenkins, A., Dutrieux, P., Jacobs, S., Mcphail, S., Perrett, J., Webb, A., and White, D.: Observations beneath Pine Island Glacier in West Antarctica and implications for its retreat, *Nature Geoscience*, 3, 468–472, <https://doi.org/10.1038/ngeo890>, 2010.
- Jenkins, A., Dutrieux, P., Jacobs, S., Steig, E., Gudmundsson, G., Smith, J., and Heywood, K.: Decadal Ocean Forcing and Antarctic Ice Sheet Response: Lessons from the Amundsen Sea, *Oceanography*, 29, 106–117, <https://doi.org/10.5670/oceanog.2016.103>, 2016.
- Joughin, I., Tulaczyk, S., Bamber, J. L., Blankenship, D., Holt, J. W., Scambos, T., and Vaughan, D. G.: Basal conditions for Pine Island and Thwaites Glaciers, West Antarctica, determined using satellite and airborne data, *Journal of Glaciology*, 55, 245–257, <https://doi.org/10.3189/002214309788608705>, 2009.
- Joughin, I., Smith, B. E., and Holland, D. M.: Sensitivity of 21st century sea level to ocean-induced thinning of Pine Island Glacier, Antarctica, *Geophysical Research Letters*, 37, <https://doi.org/10.1029/2010GL044819>, 2010.
- Joughin, I., Smith, B. E., and Schoof, C. G.: Regularized Coulomb friction laws for ice sheet sliding: application to Pine Island Glacier, Antarctica, *Geophysical research letters*, 46, 4764–4771, 2019.
- Khazendar, A., Rignot, E., and Larour, E.: Larsen B Ice Shelf rheology preceding its disintegration inferred by a control method, *Geophysical Research Letters*, 34, 1–6, <https://doi.org/10.1029/2007GL030980>, 2007.
- Lhermitte, S., Sun, S., Shuman, C., Wouters, B., Pattyn, F., Wuite, J., Berthier, E., and Nagler, T.: Damage accelerates ice shelf instability and mass loss in Amundsen Sea Embayment, *Proceedings of the National Academy of Sciences*, 117, 24 735–24 741, <https://doi.org/10.1073/pnas.1912890117>, 2020.
- MacAyeal, D. R.: Large-scale ice flow over a viscous basal sediment: Theory and application to ice stream B, Antarctica, *Journal of Geophysical Research: Solid Earth*, 94, 4071–4087, <https://doi.org/10.1029/JB094iB04p04071>, 1989.
- MacAyeal, D. R.: The basal stress distribution of ice stream E, Antarctica, inferred by control methods, *Journal of Geophysical Research*, <https://doi.org/10.1029/91JB02454>, 1992.
- McMillan, M., Shepherd, A., Sundal, A., Briggs, K., Muir, A., Ridout, A., Hogg, A., and Wingham, D.: Increased ice losses from Antarctica detected by CryoSat-2, *Geophysical Research Letters*, 41, 3899–3905, <https://doi.org/10.1002/2014GL060111>, 2014.
- Minchew, B., Simons, M., Björnsson, H., Pálsson, F., Morlighem, M., Seroussi, H., Larour, E., and Hensley, S.: Plastic bed beneath Hofsjökull Ice Cap, central Iceland, and the sensitivity of ice flow to surface meltwater flux, *Journal of Glaciology*, 62, 147–158, <https://doi.org/10.1017/jog.2016.26>, 2016.

- Morlighem, M., Rignot, E., Binder, T., Blankenship, D., Drews, R., Eagles, G., Eisen, O., Ferraccioli, F., Forsberg, R., Fretwell, P., Goel, V., Greenbaum, J. S., Gudmundsson, H., Guo, J., Helm, V., Hofstede, C., Howat, I., Humbert, A., Jokatz, W., Karlsson, N. B., Lee, W. S., Matsuoka, K., Millan, R., Mouginot, J., Paden, J., Pattyn, F., Roberts, J., Rosier, S., Ruppel, A., Seroussi, H., Smith, E. C., Steinhage, D., Sun, B., den Broeke, M. R., Ommen, T. D., van Wessem, M., and Young, D. A.: Deep glacial troughs and stabilizing ridges unveiled beneath the margins of the Antarctic ice sheet, *Nature Geoscience*, 13, 132–137, <https://doi.org/10.1038/s41561-019-0510-8>, <http://dx.doi.org/10.1038/s41561-019-0510-8>, 2020.
- Mouginot, J., Rignot, E., and Scheuchl, B.: Sustained increase in ice discharge from the Amundsen Sea Embayment, West Antarctica, from 1973 to 2013, *Geophysical Research Letters*, 41, 1576–1584, 2014.
- Mouginot, J., Rignot, E., and Scheuchl, B.: MEaSUREs Phase-Based Antarctica Ice Velocity Map, Version 1., <https://doi.org/https://doi.org/10.5067/PZ3NJ5RXRH10>, last accessed 10/2019, 2019a.
- Mouginot, J., Rignot, E., and Scheuchl, B.: Continent-Wide, Interferometric SAR Phase, Mapping of Antarctic Ice Velocity, *Geophysical Research Letters*, 46, 9710–9718, <https://doi.org/10.1029/2019GL083826>, 2019b.
- Nilsson, J., Gardner, A., Sørensen, L. S., and Forsberg, R.: Improved retrieval of land ice topography from CryoSat-2 data and its impact for volume-change estimation of the Greenland Ice Sheet, *Cryosphere*, 10, 2953–2969, <https://doi.org/10.5194/tc-10-2953-2016>, 2016.
- Padman, L., Fricker, H. A., Coleman, R., Howard, S., and Erofeeva, L.: A new tide model for the Antarctic ice shelves and seas, *Annals of Glaciology*, 34, 247–254, <https://doi.org/10.3189/172756402781817752>, 2002.
- Padman, L., King, M., Goring, D., Corr, H., and Coleman, R.: Ice-shelf elevation changes due to atmospheric pressure variations, *Journal of Glaciology*, 49, 521–526, <https://doi.org/10.3189/172756503781830386>, 2004.
- Paolo, F., Padman, L., Fricker, H., Adusumilli, S., Howard, S., and Siegfried, M.: Response of Pacific-sector Antarctic ice shelves to the El Niño/Southern Oscillation, *Nature Geoscience*, 1, <https://doi.org/10.1038/s41561-017-0033-0>, 2018.
- Paolo, F. S., Fricker, H. A., and Padman, L.: Constructing improved decadal records of Antarctic ice shelf height change from multiple satellite radar altimeters, *Remote Sensing of Environment*, 177, 192–205, <https://doi.org/10.1016/j.rse.2016.01.026>, 2016.
- Payne, A. J., Vieli, A., Shepherd, A. P., Wingham, D. J., and Rignot, E.: Recent dramatic thinning of largest West Antarctic ice stream triggered by oceans, *Geophysical Research Letters*, 31, 1–4, <https://doi.org/10.1029/2004GL021284>, 2004.
- Pritchard, H., Arthern, R., Vaughan, D., and Edwards, L.: Extensive dynamic thinning on the margins of the Greenland and Antarctic Ice Sheets, *Nature*, 461, 971–5, <https://doi.org/10.1038/nature08471>, 2009.
- Pritchard, H., Ligtenberg, S., Fricker, H., Vaughan, D., Van den Broeke, M., and Padman, L.: Antarctic ice-sheet loss driven by basal melting of ice shelves, *Nature*, 484, 502–5, <https://doi.org/10.1038/nature10968>, 2012.
- Reese, R., Gudmundsson, G. H., Levermann, A., and Winkelmann, R.: The far reach of ice-shelf thinning in Antarctica, *Nature Climate Change*, 8, 53–57, <https://doi.org/10.1038/s41558-017-0020-x>, <http://dx.doi.org/10.1038/s41558-017-0020-x>, 2018.
- Rignot, E.: Changes in West Antarctic ice stream dynamics observed with ALOS PALSAR data, *Geophysical Research Letters*, 35, <https://doi.org/10.1029/2008GL033365>, 2008.
- Rignot, E., Vaughan, D. G., Schmeltz, M., Dupont, T., and Macayeal, D.: Acceleration of Pine Island and Thwaites Glaciers, West Antarctica, *Annals of Glaciology*, 34, 189–194, <https://doi.org/10.3189/172756402781817950>, 2002.
- Rignot, E., Mouginot, J., and Scheuchl, B.: Ice Flow of the Antarctic Ice Sheet, *Science*, 333, 1427–1430, <https://doi.org/10.1126/science.1208336>, <https://www.sciencemag.org/lookup/doi/10.1126/science.1208336>, 2011.
- Rignot, E., Mouginot, J., Morlighem, M., Seroussi, H., and Scheuchl, B.: Widespread, rapid grounding line retreat of Pine Island, Thwaites, Smith, and Kohler glaciers, West Antarctica, from 1992 to 2011, *Geophysical Research Letters*, 41, 3502–3509, 2014.

- Rosier, S., Reese, R., Donges, J., De Rydt, J., Gudmundsson, G., and Winkelmann, R.: The tipping points and early-warning indicators for Pine Island Glacier, West Antarctica, <https://doi.org/10.31223/osf.io/y95r6>, 2020.
- Schmeltz, M., Rignot, E., Dupont, T. K., and Macayeal, D. R.: Sensitivity of Pine Island Glacier, West Antarctica, to changes in ice-shelf and basal conditions: A model study, *Journal of Glaciology*, 48, 552–558, <https://doi.org/10.3189/172756502781831061>, 2002.
- Schoof, C.: Variational methods for glacier flow over plastic till, *Journal of Fluid Mechanics*, 555, 299–320, <https://doi.org/10.1017/S0022112006009104>, 2006.
- Seroussi, H., Morlighem, M., Rignot, E., Mouginot, J., Larour, E., Schodlok, M., and Khazendar, A.: Sensitivity of the dynamics of Pine Island Glacier, West Antarctica, to climate forcing for the next 50 years, *Cryosphere*, 8, 1699–1710, [https://doi.org/10.5194/tc-8-1699-](https://doi.org/10.5194/tc-8-1699-2014) 2014, 2014.
- Shepherd, A., Wingham, D., Mansley, J., and Corr, H.: Inland Thinning of Pine Island Glacier, West Antarctica, *Science* (New York, N.Y.), 291, 862–4, <https://doi.org/10.1126/science.291.5505.862>, 2001.
- Shepherd, A., Wingham, D., and Rignot, E.: Warm ocean is eroding West Antarctic ice sheet. *Geophys Res Lett* 31(L23):402, *Geophysical Research Letters*, 31, <https://doi.org/10.1029/2004GL021106>, 2004.
- Shepherd, A., Hogg, A., Muir, A., and McMillan, M.: Surface Elevation Changes of the Antarctic Ice Sheet from Satellite Radar Altimetry, Antarctic-CCI-SEC-v1.0, 2016.
- Smith, J. A., Andersen, T. J., Shortt, M., Gaffney, A., Truffer, M., Stanton, T., Bindschadler, R., Dutrieux, P., Jenkins, A., Hillenbrand, C.-D., et al.: Sub-ice-shelf sediments record history of twentieth-century retreat of Pine Island Glacier, *Nature*, 541, 77–80, 2017.
- Steig, E., Ding, Q., Battisti, D., and Jenkins, A.: Tropical forcing of Circumpolar Deep Water Inflow and outlet glacier thinning in the Amundsen Sea Embayment, West Antarctica, *Annals of Glaciology*, 53, 19–28, <https://doi.org/10.3189/2012AoG60A110>, 2012.
- Sun, S., Cornford, S. L., Moore, J. C., Gladstone, R., and Zhao, L.: Ice shelf fracture parameterization in an ice sheet model, *Cryosphere*, 11, 2543–2554, <https://doi.org/10.5194/tc-11-2543-2017>, 2017.
- Tsai, V. C., Stewart, A. L., and Thompson, A. F.: Marine ice-sheet profiles and stability under Coulomb basal conditions, *Journal of Glaciology*, 61, 205–215, <https://doi.org/10.3189/2015JoG14J221>, 2015.
- Tulaczyk, S., Kamb, W. B., and Engelhardt, H. F.: Basal mechanics of Ice Stream B, west Antarctica: 1. Till mechanics, *Journal of Geophysical Research: Solid Earth*, 105, 463–481, <https://doi.org/10.1029/1999JB900329>, 2000.
- Vieli, A., Payne, A. J., Shepherd, A., and Du, Z.: Causes of pre-collapse changes of the Larsen B ice shelf: Numerical modelling and assimilation of satellite observations, *Earth and Planetary Science Letters*, 259, 297–306, <https://doi.org/10.1016/j.epsl.2007.04.050>, 2007.
- Weertman, J.: On the sliding of glaciers, *Journal of glaciology*, 3, 33–38, 1957.
- Zoet, L. K. and Iverson, N. R.: A slip law for glaciers on deformable beds, *Science*, 368, 76–78, <https://doi.org/10.1126/SCIENCE.AAZ1183>, 2020.